

1 **Revision 3 (correction date 08/19/2021)**

2 **The efficiency of copper extraction from magma bodies:**
3 **Implications for mineralization potential and fluid-silicate melt**
4 **partitioning of copper**

5 **JIN-SHENG ZHOU¹, QIANG WANG^{1,2,3,*}, DEREK A. WYMAN⁴, ZHEN-HUA**
6 **ZHAO⁵, LE ZHANG¹, PENG-LI HE¹**

7 ¹State Key Laboratory of Isotope Geochemistry, Guangzhou Institute of Geochemistry, Chinese Academy
8 of Sciences, Guangzhou 510640, China

9 ²CAS Center for Excellence in Tibetan Plateau Earth Sciences, Beijing 100101, China

10 ³College of Earth and Planetary Sciences, University of Chinese Academy of Sciences, Beijing 100049,
11 China

12 ⁴School of Geosciences, University of Sydney, NSW 2006, Australia

13 ⁵Key laboratory of Mineralogy and Metallogeny, Guangzhou Institute of Geochemistry, Chinese Academy
14 of Sciences, Guangzhou 510640, China

15
16
17 Corresponding author: Qiang Wang

18 E-mail address: wqiang@gig.ac.cn

19 Full postal address: Kehua Street 511, Guangzhou, China, 510640

20
21
22

23

ABSTRACT

24 Multiple factors may downgrade the mineralization potential of an intermediate-felsic
25 intrusion, such as the commonly invoked inefficient fluid exsolution and lack of ore-forming
26 species (metals and their ligands) in magmas. However, other factors may affect
27 mineralization potential of a magma body but have poorly understood roles in the formation
28 of magmatic-hydrothermal ore deposits. Here, we present a comparison between two Cu
29 mineralizing plutons and a Cu-poor, Fe mineralizing pluton in the Edong district. Efficient
30 fluid exsolution and extraction occurred during the solidification of all three plutons, as
31 evidenced by extensive skarn alteration around them. The results show that the oxidation state
32 of the three plutons is similar (within a range of $\sim\Delta\text{NNO} +0.9$ to $\Delta\text{NNO} +2.5$). A systematic
33 comparison of the Cu contents of a certain suite of minerals of the three plutons show that the
34 Cu concentrations of all minerals in the Cu mineralizing plutons are lower than those of the
35 Cu-poor Fe mineralizing pluton. This indicates that the Cu mineralizing plutons underwent
36 more efficient copper extraction. Thus, igneous crystals with anomalously low Cu contents
37 may potentially be used as a tool to identify Cu mineralizing magmatic units in a deposit with
38 multiphase intrusions. We suggest that the inefficient copper extraction from plutons may be
39 ascribed to the lack of reduced S species during fluid exsolution or different evolution paths
40 of Cu and Cl during magma crystallization.

41 **Keywords:** geothermobarometry, fluid exsolution, copper deposit, magma, ore-forming
42 potential

43

44

45

INTRODUCTION

46

47

48

49

50

51

52

53

54

55

56

57

58

59

60

61

62

63

64

65

66

Magmatic-hydrothermal ore deposits, including porphyry (Cooke et al. 2005; Seedorff et al. 2005; Sillitoe 2010), skarn (Meinert et al. 2005; Chang et al. 2019) and epithermal type deposits (Hedenquist et al. 1998; Simmons et al. 2005), are the primary source of copper for our society (Arndt et al. 2017). There is a consensus that intermediate-felsic intrusions provide most of the copper, chlorine, and water that are necessary to produce hydrothermal alteration and ore bodies in porphyry copper systems and associated skarns (Hedenquist and Lowenstern 1994; Candela 1997; Meinert et al. 2003; Richards 2003; Williams-Jones and Heinrich 2005; Sillitoe 2010; Audétat and Simon 2012). The formation of porphyry Cu deposits and associated skarns potentially involves multiple processes (Richards 2013; Wilkinson 2013), such as a contribution from oxidized mantle (e.g., Mungall 2002; Wang et al. 2006), pre-enrichment in the lower crust (e.g., Lee et al. 2012; Chiaradia 2014; Hou et al. 2015; Chiaradia and Caricchi 2017; Zheng et al. 2019), sulfide saturation in shallow magma bodies (e.g., Wilkinson 2013), injection of mafic magmas (e.g., Blundy et al. 2015; Yang et al. 2015; Cao et al. 2018), focused fluid flow, and repetitive fluid injections (e.g., Mercer et al. 2015; Li et al. 2017). There is growing evidence supporting the view that magma bodies with typical concentrations of metals (e.g., ~50–100 ppm Cu) may sustain the formation of economic ore deposits (Cline and Bodnar, 1991; Chelle-Michou et al. 2017; Zhang and Audétat 2017, 2018), because most metals have high fluid/melt partition coefficients, leading to significant enrichment of them in exsolved fluids (Zajacz et al., 2008; Audétat 2019). On the basis of this hypothesis, if efficient fluid exsolution occurs, many intermediate-felsic intrusions should have an ability to form economic Cu deposits. Nevertheless, many plutons

67 showing efficient fluid exsolution also lack Cu mineralization, indicating that other factors
68 may suppress the mineralization potential of intrusions. Whole-rock analyses may not be
69 sufficient to provide a better understanding of this question, because some fraction of the
70 metals and volatiles in an intrusion are commonly lost after solidification. Comparison of
71 melt inclusion compositions from barren and mineralized plutons could provide important
72 insights into this question, but available data sets show that there is no obvious difference in
73 metal concentrations between barren and mineralizing melts (e.g., Audétat 2015; Zhang and
74 Audétat 2017, 2018). It is noteworthy that the studied barren plutons contain abundant
75 miarolitic cavities that represent fluid pockets, implying inefficient extraction of the fluids
76 out of the magma (e.g., Audétat and Pettko 2003; Zhang and Audétat 2018). It is thus
77 difficult to distinguish whether the lack of mineralization is ascribed to inefficient fluid
78 extraction or other factors.

79 Here, we present a study of minerals (clinopyroxene, feldspar, amphibole, titanite and
80 apatite) from intrusions associated with the Tonglushan Cu-Fe-Au (1.08 Mt Cu, 60 Mt Fe, 70
81 t Au and 508 t Ag; Li et al., 2014), Tieshan Fe-Cu (160 Mt Fe and 0.67 Mt Cu; Li et al.
82 2014), and Jinshandian Fe (200 Mt Fe; Zhu et al. 2015, 2017) skarns in the Edong district
83 (East China), which is one of the most productive Cu-Fe provinces in China. Extensive skarn
84 alteration has been found around all three plutons, indicating that efficient fluid exsolution
85 and extraction occurred during their solidification. A comparison of the three plutons
86 provides an opportunity to identify potential factors that downgrade the Cu-mineralizing
87 potential of an intermediate-felsic intrusion. Our results suggest that the efficiency of copper
88 extraction from magma bodies by fluids plays a critical role in determining Cu

89 mineralization potential.

90

91

GEOLOGICAL BACKGROUND

92 The three studied skarn deposits are located in the Edong district, which is situated on the
93 northern margin of the Yangtze Craton (Figure 1). Regional tectonic characteristics and
94 magmatism have been described by Zhou et al. (2020a). Magmatic activity in the Edong
95 district began at ~150 Ma and ceased at ~120 Ma when this area was located in an intraplate
96 setting (e.g., Wang et al. 2004; Li et al. 2008; Hou et al. 2013; Pirajno and Zhou 2015; Zhou
97 et al. 2015; Zhou et al. 2020a). Extensive hydrothermal alteration and ore deposit formation
98 accompanied the magmatism (Li et al. 2014; Zhou et al. 2020a). There are more than 70
99 economic Cu-Fe-Au-(Mo-W) deposits within the Edong district, which is a very productive
100 Cu-Fe province (Fig. 1; Li et al. 2014). Skarn and porphyry types are the main
101 alteration-mineralization styles. The skarn deposits sampled for this study which include the
102 Tonglushan Cu-Fe-Au, Tieshan Fe-Cu, and Jinshandian Fe deposits (Fig. 2), have different
103 metal endowments.

104 The Tonglushan Cu-Fe-Au skarn deposit is the largest ore deposit in the Edong district
105 and contains 1.08 Mt Cu (~1.8 wt% Cu), 60 Mt Fe (~41 wt% Fe), 70 t Au (~0.38 g/t Au) and
106 508 t Ag (Li et al. 2014). The Tonglushan deposit contains twelve ore bodies, which are
107 located at the contact zones between the quartz monzodiorite and carbonate rocks or large
108 carbonate xenoliths within the quartz monzodiorite (Fig. 2C). Most ore bodies have lenticular
109 shapes and are 200–500 m in length and 30–110 m in thickness, with vertical extents of
110 100–500 m (Yu et al. 1985). In addition, ore-bearing breccia pipes have been found at deep

111 levels (Liu et al. 2005). Skarn alteration developed both within the pluton (i.e., endoskarn)
112 and carbonate rocks (i.e., exoskarn), but ore bodies are mainly distributed in exoskarn zones
113 (Zhao et al. 2012). The minerals formed in the prograde stage are andradite, grossular,
114 diopside, hedenbergite, scapolite, and plagioclase, followed by a retrograde alteration
115 assemblage that includes epidote, actinolite, pargasite, phlogopite, chlorite, fluorite, quartz,
116 serpentine, illite, montmorillonite, kaolinite and dickite (Li et al. 2014; Chen et al. 2019). Ore
117 minerals, including magnetite, hematite, chalcopyrite, bornite, chalcocite, molybdenite, native
118 gold and electrum, are generally associated with retrograde minerals (Li et al. 2014).
119 $^{40}\text{Ar}/^{39}\text{Ar}$ dating of the phlogopite in the skarn gives an age of ~140 Ma (Li et al. 2014). The
120 quartz monzodiorite pluton has a zircon U-Pb age of 142 ± 1 Ma (Li et al. 2014). Several
121 albitite dikes cut the pluton and skarns (Fig. 2C), indicating that they were intruded after
122 mineralization.

123 The Tieshan Fe-Cu skarn deposit contains 160 Mt Fe (~53 wt% Fe) and 0.67 Mt Cu (~0.6
124 wt% Cu) (Li et al. 2014). Six large orebodies have been found along the contact between the
125 quartz diorite and carbonate rocks (Fig. 2A). Most ore bodies are 480–920 m in length and
126 10–180 m in thickness, with vertical extents of 200–700 m (Shu et al. 1992). Skarn minerals
127 include garnet, diopside, scapolite, phlogopite, actinolite, albite, plagioclase, epidote, chlorite,
128 tremolite, and pargasite (Li et al. 2014). The phlogopite within the skarns has a $^{40}\text{Ar}/^{39}\text{Ar}$ age
129 of 142 ± 3 Ma (Xie et al. 2011). The ore minerals are dominated by magnetite, pyrite,
130 chalcopyrite, pyrrhotite and hematite (Hu et al. 2017). The ore-forming pluton, the quartz
131 diorite, has a zircon U-Pb age of 140.9 ± 1.2 Ma (Xie et al. 2007).

132 The Jinshandian Fe skarn deposit is situated on the southern and western margins of the

133 Jinshandian pluton (Fig. 2B) and contains 200 Mt Fe (~42.3 wt% Fe) (Zhu et al. 2015, 2017),
134 whereas Cu and Au are absent (Shu et al. 1992). More than 130 ore bodies have been found at
135 the contact zones between the Jinshandian pluton and carbonate or clastic rocks (Fig. 2B), and
136 most of them occur as lenses and veins (Zhu et al. 2015). The skarn mineral assemblages
137 include diopside, phlogopite, scapolite, and amphibole, with minor serpentine, garnet, titanite
138 and epidote (Zhu et al. 2015). The phlogopite has a $^{40}\text{Ar}/^{39}\text{Ar}$ age of 127.6 ± 0.9 Ma (Zhu et al.
139 2017). The ore mineralogy is dominated by magnetite (Shu et al. 1992), which commonly
140 occurs with diopside and phlogopite (Zhu et al. 2017). In addition, anhydrite and pyrite also
141 exist. Anhydrite is present within country rocks, the contact zones between ore body and
142 country rocks, and retrograde skarns in the form of veins or massive aggregates (Zhu et al.
143 2017). The quartz diorite pluton has zircon U-Pb ages of 127.4 ± 1.2 Ma and 127.6 ± 0.7 Ma
144 (Zhu et al. 2017).

145 The Tieshan plutonic samples, consisting of plagioclase (40–50%), hornblende (10–15%),
146 clinopyroxene (10–15%), K-feldspar (5–10%), quartz (5–10%), and minor magnetite, biotite,
147 and titanite, are adjacent to a endoskarn zone (Fig. 2A). The Tonglushan plutonic samples,
148 containing plagioclase (50–60%), K-feldspar (10–20%), quartz (10–20%), hornblende
149 (10–20%) and minor biotite, titanite and magnetite, were collected from an old mining pit,
150 which is several hundred meters from the current mining location (Fig. 2C). The Jinshandian
151 plutonic rocks, consisting of plagioclase (30–40%), K-feldspar (20–30%), hornblende
152 (15–20%), clinopyroxene (5–10%), quartz (5–10%), and minor titanite, biotite, and magnetite,
153 are adjacent to the Jinshandian western ore bodies (Fig. 2B). The plutonic samples of the
154 Tonglushan and Tieshan deposits are the same as those reported in Zhou et al. (2020a);

155 previously analyzed samples. All analyses of Jinshandian deposit samples are new. Minerals
156 with homogeneous interiors or regular zoning patterns that indicate magmatic origin were
157 selected for major and trace element analyses. Some secondary titanite crystals were also
158 analyzed for comparison.

159

160 **ANALYTICAL METHODS**

161 **Whole-rock compositional analysis**

162 Whole-rock major element analyses were performed using X-ray fluorescence
163 spectrometry at Hubei Institute of Geology and Mineral Resource, with analytical errors less
164 than 2 %. Whole-rock trace element analyses were performed using a Perkin-Elmer ELAN
165 6000 inductively coupled plasma source mass spectrometer (ICP-MS) at the State Key
166 Laboratory of Isotope Geochemistry (SKLaBIG), Guangzhou Institute of Geochemistry,
167 Chinese Academy of Sciences (GIG-CAS). The analytical procedures are similar to Li et al.
168 (2002), with an analytical precision better than 2%.

169

170 **Mineral compositional analysis**

171 Major element abundances in minerals were analyzed on a JEOL JXA 8100 Superprobe
172 with a 15 kV accelerating voltage, 20 nA beam current, 2 μm probe diameter, at the SKLaBIG,
173 GIG-CAS, and a JEOL JXA 8230 electron probe micro-analyzer (EPMA) with a 15 kV
174 accelerating voltage, 20 nA beam current, 1 μm probe diameter, at the Key Laboratory of
175 Mineralogy and Metallogeny of Guangzhou Institute of Geochemistry, GIG-CAS. The EPMA
176 was calibrated using natural and synthetic standards and analytical results were reduced using

177 the ZAF (Z: atomic number; A: absorption; F: fluorescence) correction routines.

178 Mineral trace element analyses were performed using an ELEMENT XR (Thermo Fisher
179 Scientific) inductively coupled plasma sector field mass spectrometry (ICP-SF-MS) coupled
180 with a 193-nm (ArF) Resonetics RESOLUTION M-50 laser ablation system (LA) in the
181 SKLaBIG, GIG-CAS. All LA-ICP-SF-MS spots was located to overlap a conjugate EMPA
182 spot. The spot size was 33 μm , at a pulse energy of $\sim 4 \text{ J cm}^{-2}$ and a laser repetition rate of 5
183 Hz. A smoothing device (The Squid, Laurin Technic) was used to smooth the sample signal.
184 For each spot, counting times were 20 s for gas blank collection (laser off) and 30 s for
185 sample signal detection (laser on). The standards, BCR-2G, BHVO-2G and GSD-1G, were
186 analyzed for the construction of the calibration line. Trace element concentrations were
187 normalized to that of SiO_2 , as determined by EPMA. The TB-1G (USGS reference glass) was
188 analyzed as an unknown sample and the results are shown in Appendix Table A7. For apatite,
189 NIST SRM 610 and 612 were analyzed for the calibration and unknown, respectively, and
190 CaO was used as the internal standard. More detailed experimental procedures and data
191 reduction strategies have been described by Zhang et al. (2019).

192

193 **High resolution X-ray element mapping**

194 High resolution X-ray element mapping was employed to image the zoning patterns of
195 titanite, using a Cameca SXFiveFE electron microprobe at the SKLaBIG, GIG-CAS. The
196 operating conditions were 20 kV accelerating voltage and 80 nA beam current.

197

198

RESULTS

199 All of the whole-rock and mineral data used in this study can be found in Appendix Table
200 A1 to A6, including data previously published in Zhou et al. (2020a). Representative
201 whole-rock and mineral data are shown in Tables 1–6. The majority of mineral major and
202 trace element analyses both in this study and Zhou et al. (2020a) were performed at the
203 SKLaBIG, GIG-CAS.

204 **Whole-rock compositions**

205 The representative whole-rock chemical compositions of the Tonglushan, Tieshan and
206 Jinshandian plutonic rocks are in Table 1 and the full list of analyses are provided in Appendix
207 Table A1. The Tonglushan plutonic rocks have $\text{SiO}_2 = 62.6\text{--}63.7$ wt%, $\text{MgO} = 0.86\text{--}1.44$ wt%,
208 $\text{Na}_2\text{O} = 4.35\text{--}4.53$ wt%, $\text{K}_2\text{O} = 2.71\text{--}2.75$ wt%, and $\text{Mg\#} = 26.0\text{--}36.9$. For trace elements of
209 interest, concentrations or ratios are, respectively: $\text{Zr} = 131$ ppm; $\text{Sr} = 961\text{--}983$ ppm; $\text{Y} =$
210 $17.0\text{--}18.3$ ppm; $\text{Eu}/\text{Eu}^* = 0.92\text{--}0.94$ ppm; Dy/Dy^* , defined as $\text{Dy}/(\text{Dy}^*) =$
211 $\text{Dy}_N/(\text{La}_N^{(4/13)} * \text{Yb}_N^{(9/13)})$ (Davidson et al., 2013), $= 0.52\text{--}0.54$; $(\text{La}/\text{Yb})_N = 21.1\text{--}21.7$. The
212 Tieshan intrusion $\text{SiO}_2 = 62.4\text{--}64.7$ wt%, $\text{MgO} = 1.42\text{--}1.92$ wt%, $\text{Na}_2\text{O} = 4.84\text{--}5.60$ wt%,
213 $\text{K}_2\text{O} = 2.67\text{--}3.30$ wt%, and $\text{Mg\#} = 39.7\text{--}47.1$. Trace element concentrations or ratios include:
214 $\text{Zr} = 79\text{--}200$ ppm; $\text{Sr} = 1337\text{--}2310$ ppm; $\text{Y} = 13.3\text{--}16.8$ ppm; $\text{Eu}/\text{Eu}^* = 0.88\text{--}1.02$ ppm;
215 $\text{Dy}/\text{Dy}^* = 0.55\text{--}0.64$; $(\text{La}/\text{Yb})_N = 23.1\text{--}33.9$. The Jinshandian quartz diorites have $\text{SiO}_2 =$
216 $58.1\text{--}71.0$ wt%, $\text{MgO} = 0.40\text{--}1.71$ wt%, $\text{Na}_2\text{O} = 2.53\text{--}9.70$ wt%, $\text{K}_2\text{O} = 0.18\text{--}4.91$ wt%, and
217 $\text{Mg\#} = 21.5\text{--}59.6$. Trace elements concentrations or ratios include: $\text{Zr} = 98.2\text{--}415$ ppm; $\text{Sr} =$
218 $129\text{--}392$ ppm; $\text{Y} = 14.0\text{--}36.2$ ppm; $\text{Eu}/\text{Eu}^* = 0.50\text{--}1.03$ ppm; $\text{Dy}/\text{Dy}^* = 0.47\text{--}0.60$; $(\text{La}/\text{Yb})_N$
219 $= 8.3\text{--}28.7$.

220

221 **Mineral major and trace element compositions**

222 **Clinopyroxene**

223 Clinopyroxene is present in the Tieshan and Jinshandian plutons, but no clinopyroxene
224 crystal has been found in the Tonglushan samples. Most of the Tieshan clinopyroxene crystals
225 are small in size (100–500 μm in length) and most of them are euhedral. Compositionally,
226 they are diopside and in the range of $\text{Wo}_{47-49}\text{En}_{36-38}\text{Fs}_{14-17}$, with Mg\# [$\text{Mg}/(\text{Mg}+\text{Fe}_{\text{total}})$] of
227 70–74 (Zhou et al. 2020a). For certain trace elements of interest, concentrations are: Cu =
228 0.02–0.94 ppm; Mo = 0.01–0.74 ppm; Zn = 166–210 ppm; Pb = 0.50–7.26 ppm; Sr =
229 19.7–58.3 ppm. The Jinshandian clinopyroxene crystals are 100–800 μm in length with a
230 euhedral morphology and most are diopside with compositions of $\text{Wo}_{49-53}\text{En}_{36-42}\text{Fs}_{8-14}$ and
231 Mg\# of 69–76. They have Cu = 0.65–0.93 ppm, Zn = 132–179 ppm, Pb = 0.61–1.96 ppm, and
232 Sr = 34.6–85.4 ppm.

233

234 **Feldspar**

235 Feldspar group minerals are the most common phase in the three plutons. Most
236 Tonglushan and Tieshan plagioclase show normal zoning or oscillatory zoning and the cores
237 are in equilibrium with their whole-rock compositions (Zhou et al. 2020a). Setting aside the
238 compositional zoning, the plagioclase An values of the Tonglushan, Tieshan, and Jinshandian
239 plutons are An_{20-58} , An_{10-44} , and An_{14-30} . Concentrations of certain trace elements for the
240 Tonglushan, Tieshan, and Jinshandian plagioclase are: Cu = 0.06–1.31, 0.03–1.80 and
241 10.5–12.1 ppm; Zn = 3.16–46.8, 0.56–44.1 and 2.68–5.48 ppm; Pb = 2.90–9.30, 1.04–35.2
242 and 2.82–12.8 ppm; Sr = 1088–2752, 1396–4927 and 1605–2962 ppm. A small number of

243 analyses shows that the Tieshan and Jinshandian K-feldspar crystals have Cu of 0.04–1.80
244 and 1.81–13.0 ppm, respectively.

245

246 **Amphibole**

247 Amphibole is present in all three plutons. Most amphibole crystals in the Tonglushan
248 pluton are euhedral, with sizes ranging from 0.2 to 1.6 mm in length. Some amphibole
249 crystals contain titanite and apatite inclusions. Compositionally, the Tonglushan amphibole
250 crystals have Mg# of 62–72, Cu = 0.08–1.15 ppm, Mo = 0.06–1.14 ppm, Zn = 125–220 ppm,
251 Sr = 9.17–32.9 ppm. Two amphibole populations (euhedral vs. anhedral grains) may be
252 recognized in the Tieshan pluton (Figs. 3E and D). Some amphibole has a close spatial
253 relationship with clinopyroxene and they are in contact. Compositions for the euhedral and
254 anhedral amphibole crystals are: Mg# = 62–73 and 60–69; Cu = 0.1–2.06 and 0.03–1.01 ppm;
255 Mo = 0.01–2.07 and 0.01–0.55 ppm; Zn = 65.7–380 and 276–395 ppm; Sr = 26.4–294 and
256 18.1–73.6 ppm. Similarly, either euhedral and anhedral amphibole populations may be
257 identified in the Jinshandian pluton. Euhedral and anhedral amphibole crystals occur in
258 different hand samples and have Mg# = 57–85 and 57–73, Cu = 3.32–5.28 and 1.39–2.35 ppm,
259 Zn = 152–225 and 260–292 ppm, and Sr = 7.92–51.5 and 15.1–62.4 ppm, respectively.

260

261 **Titanite**

262 Titanite is present in the host plutons of all three deposits (Fig. 3). Titanite grains in the
263 Tieshan pluton are interstitial, but the small sizes make microanalysis difficult (Fig. 3C).
264 Analyzed titanite crystals in this study are from the Tonglushan and Jinshandian plutons. On

265 the basis of a combination of back-scattered electron images and crystal morphologies,
266 titanite crystals may be divided into magmatic and secondary crystals. One population of
267 titanite commonly exhibit oscillatory zoning (Figs. 3A and B), sector zoning, or superimposed
268 oscillatory zoning on sector zoning (Fig. 3B), which are interpreted as magmatic textures
269 (Paterson and Stephens 1992). A second population of titanite show no regular zoning patterns
270 and commonly contain Fe-Ti oxide inclusions with irregular shapes (Fig. 3F); this population
271 is interpreted as secondary. Compositionally, the titanite crystals from the Tonglushan pluton
272 have Cu = 1.83–3.61 ppm, Mo = 38.9–134 ppm, Zn = 4.68–24.4 ppm, Sr = 2.35–53.6 ppm, Cr =
273 = 6.81–19.9 ppm, and Zr = 325–3929 ppm. In the Jinshandian pluton, the magmatic titanite
274 crystals contain Cu = 5.59–6.69 ppm, Zn = 11.0–13.3 ppm, Sr = 44.0–72.0 ppm, Cr =
275 5.55–15.8 ppm, and Zr = 849–7209 ppm, and the secondary titanite crystals have Cu =
276 5.78–6.66 ppm, Zn = 12.0–13.5 ppm, Sr = 71.2–147 ppm, Cr = 87.0–303 ppm, and Zr =
277 760–2780 ppm. It is noteworthy that magmatic titanite crystals show sector zoning, because
278 this feature exerts important controls on trace element concentrations (Paterson and Stephens
279 1992).

280

281 **Apatite**

282 Apatite is a minor but ubiquitous phase in the Tonglushan, Tieshan, and Jinshandian
283 plutons. Apatite inclusions commonly occur in other minerals but most grains in the
284 Tonglushan pluton are bigger than those in the other two plutons (Fig. 3A). The larger sizes
285 (up to 200 μm in length) make microbeam analysis of the Tonglushan apatite crystals feasible.
286 Most Tonglushan apatite crystals are fluorapatite, with F = 2.85–3.69 wt%. They have Cu =

287 0.03–0.70 ppm, Zn = 0.09–3.19 ppm, Sr = 427–517 ppm, La = 1726–3959 ppm, and Y =
288 148–403 ppm.

289

290

DISCUSSION

291

Comparison of the magma properties of the three plutons

292

293

294

295

296

297

298

299

300

301

302

303

304

305

306

307

308

Magma properties play a key role in the formation of magmatic-hydrothermal ore deposits (Hedenquist and Lowenstern 1994; Audétat and Simon 2012). For example, hydrous, oxidized, and S-rich magmas are favorable for producing porphyry copper systems and associated skarns (Sillitoe 2010, 2018). The Tonglushan, Tieshan, and Jinshandian plutons contain abundant amphibole crystals, which record various intensive parameters and have important implications for magmatic processes (e.g., Zhou et al. 2020b). Several thermobarometers were used to estimate the SiO₂ contents of the melt that was in equilibrium with the crystallizing amphibole crystals and the water content, oxygen fugacity, and temperature of the magmas (Fig. 4) (Ridolfi et al. 2010; Putirka 2016). The results show that the Tonglushan, Tieshan, and Jinshandian amphibole crystals crystallized from melts with SiO₂ contents of 72.4–75.2, 71.6–75.8, and 72.1–78.9 wt%, and in temperature ranges of 725–809, 695–801, and 720–795 °C, respectively. These relatively low crystallization temperatures and high-silica equilibrium melts, compared to bulk-rock abundances, indicate that the precipitation of amphibole crystals occurred in the late stages during the solidification of the three plutons, consistent with the fact that igneous rocks in the Edong district are the products of an initially water-poor intraplate environment (Wang et al. 2004; Zhou et al. 2020a). A decrease in SiO₂ contents in equilibrium melts with decreasing temperature (Fig. 4A) suggests that amphibole

309 crystallization was accompanied by quartz crystallization (Fig. 3D). High magmatic water
310 contents are essential for ore deposit genesis, because fluid saturation and exsolution are key
311 steps in the mineralization processes (Hedenquist and Lowenstern 1994; Candela 1997;
312 Candela and Piccoli 2005; Zajacz et al. 2008; Audétat and Simon 2012; Wang et al. 2014).
313 Application of the amphibole hygrometer (Ridolfi et al. 2010) shows that the Tonglushan and
314 Tieshan amphibole crystals crystallized from melts with H₂O contents of 3.4–4.4 and 3.2–4.6
315 wt%, respectively (Fig. 4B; Zhou et al. 2020a). The anhedral amphibole crystals in the
316 Jinshandian pluton record magmatic H₂O contents of 2.9–3.9 wt%, whereas euhedral
317 amphibole crystals crystallized from the melts with H₂O contents of 0.8–2.0 wt% (Fig. 4B).
318 The H₂O contents in the melts that crystallized the Jinshandian euhedral amphibole crystals
319 increased with decreasing temperature, whereas the H₂O contents of the melts that grew the
320 anhedral amphibole in the Jinshandian pluton, as well as amphibole in the Tonglushan and
321 Tieshan, remained approximately constant with cooling (Fig. 4B). In theory, H₂O is
322 incompatible during magma crystallization and will be enriched in residual melts until fluid
323 saturation and exsolution occur. The Jinshandian euhedral amphibole crystals record such a
324 crystallization-dominated trend, whereas the other amphibole trends indicate that fluid
325 exsolution accompanied their crystallization, consistent with higher magmatic water contents
326 and volatile saturation at higher degrees of pluton crystallinity.

327 Another critical intensive parameter is magmatic oxygen fugacity, which controls the
328 behavior of sulfur as well as metals during magmatic evolution (Audétat and Simon 2012;
329 Richards 2015). High oxygen fugacities are necessary for generating porphyry copper systems,
330 and reduced ilmenite-series intrusions commonly lack economic Cu mineralization (Ishihara

331 1977, 1981; Sillitoe 2018). The oxidized state of ore-forming magmas is hypothesized to be
332 inherited from subducted oceanic slabs through the transport of slab-derived, oxidized, partial
333 melts or fluids into the mantle wedge, promoting the extraction of metals and sulfur into arc
334 magmas (e.g., Mungall 2002; Evans and Tomkins 2011). In addition, the oxidation state of
335 magmas may also be modified during subsequent magmatic differentiation, leading to either
336 magnetite fractionation-induced oxidation (e.g., Lee et al. 2010) or magnetite fractionation-
337 and degassing-induced reduction (e.g., Jenner et al. 2010; Kelley and Cottrell 2012). The
338 solubility of copper in silicate melts increases with increasing oxygen fugacity (e.g., Zajacz et
339 al. 2012). More importantly, the solubility of sulfur is strongly controlled by the oxidation
340 state of magmas (Baker and Moretti 2011). The oxidizing S^{6+} is much more soluble than the
341 reducing S^{2+} , and there is a dramatic increase of the sulfur solubility in magmas at magmatic
342 oxygen fugacity greater than $\sim\Delta FMQ + 1.0$ (corresponding to $\sim\Delta NNO + 0.4$ at temperatures $<$
343 $1000\text{ }^{\circ}\text{C}$; Jugo et al. 2010). The potential of Cu mineralization is therefore suppressed in
344 magmas with low oxygen fugacities (e.g., Zajacz et al. 2012). Another possible means of
345 lowering ore-forming potential via low oxygen fugacities is the sequestration of metals by
346 early sulfide fractionation (e.g., Jenner et al. 2010; Park et al. 2015, 2019; Hao et al. 2017),
347 but this proposal is not widely accepted (e.g., Spooner 1993; Keith et al. 1997; Larocque et al.
348 2000; Halter et al. 2002, 2005; Stavast et al. 2006; Nadeau et al. 2010, 2013; Wilkinson 2013;
349 Du and Audétat 2020). Here, we employed the amphibole oxybarometer (Ridolfi et al. 2010)
350 to track the oxidation state of the three plutons. As illustrated in Figures 4C and D, the
351 amphibole crystals in the Tonglushan, Tieshan, and Jinshandian plutons record magmatic
352 oxygen fugacities ranging from $\Delta NNO + 1.0$ to $\Delta NNO + 2.5$, $\Delta NNO + 1.0$ to $\Delta NNO + 2.2$

353 (Zhou et al. 2020a; Duan et al. 2017), and $\Delta\text{NNO} +0.9$ to $\Delta\text{NNO} +2.1$, respectively. Thus,
354 there is no systematic difference in magmatic oxygen fugacity between Cu and Cu-poor Fe
355 mineralizing magmas. However, it is noteworthy that the oxygen fugacities of euhedral
356 amphibole crystals in the Jinshandian pluton decrease with cooling, whereas those of other
357 amphibole crystals increase with decreasing temperature (Fig. 4D). Combined with the
358 evolving trends of water, we can speculate that magmatic oxygen fugacities will decrease with
359 crystallization but increase with crystallization accompanying fluid exsolution.

360

361 **The efficiency of copper extraction**

362 The significant enrichment of Cu from magmas with normal concentrations of Cu
363 (~50–100 ppm) (Cline and Bodnar 1991; Richards 2015; Chelle-Michou et al. 2017; Zhang
364 and Audétat 2017) to anomalously Cu-rich fluids (Audétat 2019) may be described by fluid
365 separation due to very high fluid/melt partition coefficients (Zajacz et al. 2008; Audétat 2019).
366 Assuming that the common factors such as sulfur contents, host rocks and depths are
367 beneficial for mineralization, fluid exsolution can be observed in many shallow intrusions but
368 only a small portion of these produce Cu mineralization, suggesting that there are other
369 factors that downgrade the Cu mineralization potential of a barren intermediate-felsic
370 intrusion. The intermediate-felsic intrusions represent residual material after fluid exsolution,
371 and therefore offer clues to the mineralization potential of a given system.

372 For this purpose, we present a systematic comparison of the compositions of common
373 minerals in the Tonglushan, Tieshan, and Jinshandian plutons, including clinopyroxene,
374 plagioclase, K-feldspar, amphibole, titanite, and apatite. Two important factors should be

375 addressed before such comparisons, (1) exclusion of data that were contaminated by crystal,
376 melt and fluid inclusions; and (2) establishing the influence of disequilibrium zoning patterns
377 (such as sector zoning) on mineral compositions. Small crystals, melt and/or fluid inclusions
378 are easily trapped by large crystals during magmatic crystallization (e.g., Halter et al. 2004)
379 and their presence may affect microanalyses. Examination of the transient signals from
380 analyses is a useful approach for identifying fine-scale inclusions in minerals. All
381 microanalytical data for mineral Cu content was checked in transient signals and the data
382 showing the presence of inclusions were excluded. Another problem is the influence of the
383 zoning patterns that were produced by disequilibrium crystal growth. Unlike commonly
384 observed equilibrium zonation in igneous crystals such as normal, reverse and oscillatory
385 zoning patterns, sector zoning is a kinetically induced compositional zoning in which
386 compositionally heterogeneous domains might have crystallized from the same melt at similar
387 conditions (e.g., Zhou et al. 2021). An example of its influence on mineral compositions is
388 provided by titanite from the Tonglushan pluton (Fig. 5). Titanite (CaTiSiO_5) is a common
389 Ti-bearing accessory phase in granitoid rocks (e.g., Piccoli et al. 2000) and hydrothermal
390 systems (e.g., Chelle-Michou et al. 2015; Song et al. 2019), and has very high contents of
391 certain trace elements (e.g., REE, Y, Zr, Nb, U, Th, etc.). Due to low cation diffusivities,
392 titanite commonly develops sector zoning, even with relatively low crystal growth rates
393 (Paterson and Stephens 1992; Watson and Liang 1995; Kohn 2017). In metaluminous
394 granitoids, the crystal habit of titanite is dominated by {111} (Paterson and Stephens 1992).
395 Exactly which faces are cut depends on the angle at which the plane of the thin section
396 intersects the grain, and the resulting zoning patterns are diverse and complex. In general, the

397 dominant {111} sectors have lower grayscale values in back-scattered electron (BSE) images,
398 and lower REE, Zr, U, Pb, Nb and Y contents relative to non-{111} sectors (Paterson and
399 Stephens 1992; Kohn 2017). The results of this study show that non-{111} sectors have
400 higher P, Y, Zr, Nb, Ta, REE, Pb, and U contents than those of {111} sectors by factors of ~2.5,
401 ~2, ~3, ~5, ~6, ~2, ~3, and ~5, respectively. However, there is no pronounced difference in Cu
402 contents among different sectors. For example, in the titanite crystal in Figure 5B, the average
403 Cu contents of the {111} and non-{111} sectors are 2.70 and 2.21 ppm, respectively.
404 Although there is no experimentally determined diffusivity of Cu in titanite to date (Kohn
405 2017), high values may be inferred because the low valence of Cu facilitates its diffusion in
406 minerals compared to most other elements (Audétat et al. 2018). The lack of obvious
407 difference in Cu content among different sectors in titanite may be ascribed to the low ratios
408 of growth rate to lattice diffusivity (Watson and Liang 1995). Thus, our results indicate that
409 the influence of disequilibrium zoning on titanite Cu contents is limited. Disequilibrium
410 zoning has not been observed in other minerals.

411 The above assessment demonstrates that it is possible to make meaningful comparisons
412 between the mineral compositions of the Tonglushan, Tieshan, and Jinshandian plutons. A
413 systematic comparison of mineral Cu concentrations of the three plutons are illustrated in
414 Figure 6 and Table 7. The result shows that almost all minerals in the Jinshandian pluton have
415 higher Cu contents than those in the Tonglushan and Tieshan plutons. The Tonglushan deposit
416 contains 1.08 Mt Cu and the Tieshan deposit contains 0.67 Mt Cu, but no economic Cu ore
417 body has been found in the Jinshandian deposit. It is unlikely that the parental magmas of the
418 Jinshandian pluton are more Cu-rich than those of the Tonglushan and Tieshan plutons.

419 Higher mineral Cu contents may also be attributed to higher partition coefficients of Cu
420 between mineral and melt. However, it is implausible that all minerals in the Jinshandian
421 pluton have higher mineral-melt partition coefficients of Cu at the same time. Thus,
422 systematically lower mineral Cu contents of the Cu- mineralized plutons should be ascribed to
423 Cu being extracted from these plutons by exsolved fluids more efficiently and completely.

424

425 **Possible factors that affect the Cu-mineralizing potential**

426 At the transition from magmatic to hydrothermal processes, a key factor responsible for
427 the lack of economic mineralization in barren plutons is inefficient fluid exsolution and
428 extraction during their solidification (e.g., Zhang and Audétat 2018). On the basis of our
429 comparison of the three skarn associated plutons, that all underwent efficient fluid exsolution
430 and extraction, this study presents evidence that the minerals in Cu mineralizing plutons have
431 distinctly lower Cu concentrations and show more efficient copper extraction relative to
432 Cu-poor Fe mineralizing plutons. Our results are consistent with observations in certain other
433 porphyry copper systems. For example, in the Los Bronces-Río Blanco district (central Chile),
434 the most productive porphyry Cu province in the world (Sillitoe 2012), plagioclase
435 phenocrysts from fertile porphyries contain significantly lower Cu contents (~0.5 ppm) than
436 those from barren intrusions (~6 ppm) (Williamson et al. 2016). Collectively, these results
437 demonstrate that the efficiency of copper extraction from magmas plays a critical role in
438 determining Cu mineralization potential (e.g., Cline and Bodnar 1991; Richards 2015;
439 Chelle-Michou et al. 2017; Zhang and Audétat 2017). More significantly, extensive skarn
440 alteration also developed around the Cu-poor Jinshandian Fe mineralized pluton, excluding

441 the possibility that the lower efficiency of Cu extraction from the Jinshandian pluton was
442 caused by inefficient fluid exsolution and extraction. It is also unlikely that the initial Cu
443 contents of the Jinshandian pluton are higher than those of the other Cu-mineralized plutons.
444 There must have been other factors that downgraded the Cu-mineralizing potential of the
445 Jinshandian pluton.

446 Here we present two possible explanations for inefficient copper extraction during the
447 solidification of the Jinshandian pluton. Anionic ligands are required to transport Cu from
448 magmas into hydrothermal fluids and chloride complexes are conventionally regarded as the
449 dominant carrier of Cu in aqueous fluids (e.g., Holland 1972; Burnham 1967, 1997; Burnham
450 and Ohmoto 1980; Candela and Holland 1984). Abundant Fe skarn ore bodies around the
451 Jinshandian pluton indicate no shortage of the chloride anion (Cl^-) in the exsolving fluids
452 because iron is transported as chloride complexes in aqueous fluids (e.g., Simon et al. 2004;
453 Zajacz et al. 2008), as also evidenced by halogen-bearing minerals such as scapolite and
454 amphibole in the Jinshandian skarns (Zhu et al. 2015). In addition, many ore bodies in the
455 Jinshandian deposit are distributed within the endoskarns (Zhu et al. 2017) whose protoliths
456 are igneous rocks (Meinert et al. 2005), indicating that Cl^- was derived from the intrusion
457 rather than from the evaporate-bearing country rocks. Thus, the inefficient transport of Cu
458 from magmas into fluids is unlikely a result of a lack of Cl^- in parent magmas. Experimental
459 studies suggest that sulfur plays an important role in the transport of Cu from melts into
460 alteration-mineralization zones, particularly in exsolving magmatic vapors (e.g., Zajacz et al.
461 2008, 2011; Seo et al. 2009; Zajacz and Halter 2009). It raises a possibility that the lower
462 efficiency of copper transfer from magmas into fluids or vapors may be affected by sulfur.

463 H₂S may increase Cu partitioning between felsic melts and fluids, however, SO₂ has weak
464 effect on Cu partitioning (Tattitch and Blundy 2017). Thus, the lack of reduced S species
465 during fluid exsolution potentially suppresses the extraction of Cu from parent magmas.
466 However, a decrease in fluid-melt Cu partition coefficients caused by the lack of H₂S is still
467 limited (Tattitch and Blundy 2017). Recent studies emphasized that Cu will be extracted
468 efficiently by hypersaline liquid at low pressures and high temperatures (Blundy et al. 2021;
469 Tattitch et al. 2021), and Cu mineralization preferentially occurs when both Cu and Cl are
470 enriched in residual magmas concurrently (Tattitch et al. 2021). Thus another possible
471 explanation is that Cu and Cl evolved along different paths during the solidification of the
472 Jinshandian pluton and one of them was depleted at the point of fluid saturation.

473

474

IMPLICATIONS

475 This study presents a comparison of three contrasting types of mineralization associated
476 with plutons in the Edong district where two plutons are related to Cu mineralization and the
477 other is a Cu-poor, Fe mineralized pluton. Extensive skarn alteration around the three plutons
478 show that efficient fluid exsolution occurred during their solidification. The three plutons had
479 similar oxygen fugacities (within a range of $\sim\Delta\text{NNO} +0.9$ to $\Delta\text{NNO} +2.5$). Almost all
480 minerals in the Cu mineralizing plutons have lower Cu concentrations than those of the
481 Cu-poor Fe mineralizing pluton, indicating the Cu mineralizing plutons underwent more
482 efficient copper extraction. Thus, the efficiency of copper extraction from magmas plays a
483 critical role in determining Cu mineralization potential. Our results indicate that a variety of
484 igneous minerals with anomalously low Cu contents could potentially be used as a tool to

485 identify Cu mineralizing magma body in a deposit with multiphase intrusions, nevertheless a
486 suite of igneous mineral compositions from a region should be analyzed for comparison. Our
487 results suggest that the inefficient copper extraction from magma body may be ascribed to the
488 lack of reduced S species during fluid exsolution or different evolution paths of Cu and Cl
489 during magma crystallization.

490

491

ACKNOWLEDGMENTS

492 We are grateful to Associate Editor Prof. Callum J. Hetherington, Dr. Brian Tattitch and
493 two anonymous reviewers for helpful, insightful and constructive reviews, and Editor Prof.
494 Don R. Baker for efficient editorial handling. We thank Lin-Li Chen and Chang-Ming Xing
495 for laboratory assistance, and Jun Wang for field help.

496

497

FUNDING

498 This research was supported by the National Natural Science Foundation of China (Nos.
499 42021002, 41630208 and 91855215) and the Key Program of Guangzhou City (No.
500 201707020032). This is contribution No.×× from GIGCAS.

501

502

REFERENCES CITED

503 Arndt, N. T., Fontboté, L., Hedenquist, J. W., Kesler, S. E., Thompson, J. F., and Wood, D. G. (2017) Future
504 global mineral resources. *Geochemical Perspectives*, 6, 1–171.
505 Audétat, A. (2015) Compositional evolution and formation conditions of magmas and fluids related to
506 porphyry Mo mineralization at Climax, Colorado. *Journal of Petrology*, 56, 1519–1546.

- 507 Audétat, A. (2019) The Metal Content of Magmatic-Hydrothermal Fluids and Its Relationship to
508 Mineralization Potential: *Economic Geology*, 114, 1033–1056.
- 509 Audétat, A., and Pettke, T. (2003) The magmatic-hydrothermal evolution of two barren granites: a melt and
510 fluid inclusion study of the Rito del Medio and Cañada Pinabete plutons in northern New Mexico
511 (USA). *Geochimica et Cosmochimica Acta*, 67, 97–121.
- 512 Audétat, A. and Simon, A. C. (2012) Magmatic controls on porphyry copper genesis, in Hedenquist, J. W.,
513 Harris, M. and Camus F., ed., *Geology and Genesis of Major Copper Deposits and Districts of the*
514 *world: A Tribute to Richard H. Sillitoe*. Society of Economic Geologists, Special Publication 16,
515 553–572.
- 516 Audétat, A., Zhang, L., and Ni, H. (2018) Copper and Li diffusion in plagioclase, pyroxenes, olivine and
517 apatite, and consequences for the composition of melt inclusions. *Geochimica et Cosmochimica Acta*,
518 243, 99–115.
- 519 Baker, D. R., and Moretti, R. (2011) Modeling the Solubility of Sulfur in Magmas: A 50-Year Old
520 Geochemical Challenge. *Reviews in Mineralogy and Geochemistry*, 73, 167–213.
- 521 Blundy, J., Mavrogenes, J., Tattitch, B., Sparks, S., and Gilmer, A. (2015) Generation of porphyry copper
522 deposits by gas–brine reaction in volcanic arcs. *Nature Geoscience*, 8, 263–269.
- 523 Blundy, J., Afanasyev, A., Tattitch, B., Sparks, S., Melnik, O., Utkin, I., and Rust, A. (2021) The economic
524 potential of metalliferous sub-volcanic brines. *Royal Society Open Science*, 8, 202192.
- 525 Burnham, C.W. (1967) Hydrothermal fluids at the magmatic stage, in Barnes, H.L., ed., *Geochemistry of*
526 *hydrothermal ore deposits*: New York, Holt, Rinehart and Winston, p. 34–76.
- 527 Burnham, C.W. (1997) *Magmas and hydrothermal fluids*, in Barnes, H.L., ed., *Geochemistry of*
528 *hydrothermal ore deposits*, 3rd ed.: New York, John Wiley & Sons, p. 63–123.

- 529 Burnham, C.W. and Ohmoto, H. (1980) Late-stage processes of felsic magmatism: Mining Geology Special
530 Issue 8, p. 1–11.
- 531 Candela, P. A. (1997) A Review of Shallow, Ore-related Granites: Textures, Volatiles, and Ore Metals.
532 Journal of Petrology, 38, 1619–1633.
- 533 Candela, P. A., and Holland, H. D. (1984) The partitioning of copper and molybdenum between silicate
534 melts and aqueous fluids. *Geochimica et Cosmochimica Acta*, 48, 373–380.
- 535 Candela, P. A. and Piccoli, P. M. (2005) Magmatic processes in the development of porphyry-type ore
536 systems, in Hedenquist, J. W., Thompson, J. F. H., Goldfarb, R. J. and Richards, J. P., ed., *Economic
537 Geology 100th Anniversary Volume: Society of Economic Geologists*, Littleton, Colorado, 25–37.
- 538 Cao, M.J., Hollings, P., Cooke, D.R., Evans, N.J., McInnes, B.I.A., Qin, K.Z., Li, G.M., Sweet, G., and
539 Baker, M. (2018a) Physicochemical processes in the magma chamber under the Black Mountain
540 porphyry Cu-Au deposit (Philippines): Insights from mineral chemistry and implications for
541 mineralization. *Economic Geology*, 113, 63–82.
- 542 Chang, Z., Shu, Q., and Meinert, L. D. (2019) Skarn Deposits of China, in Chang, Z. and Goldfarb R. J.,
543 ed., *Mineral deposits of China*. Society of Economic Geologists, Special Publication 22, 189–234.
- 544 Chelle-Michou, C., Chiaradia, M., Selby, D., Ovtcharova, M., and Spikings, R. A. (2015) High-Resolution
545 Geochronology of the Coroccohuayco Porphyry-Skarn Deposit, Peru: A Rapid Product of the Incaic
546 Orogeny. *Economic Geology*, 110, 423–443.
- 547 Chelle-Michou, C., Rottier, B., Caricchi, L., and Simpson, G. (2017) Tempo of magma degassing and the
548 genesis of porphyry copper deposits. *Scientific Reports*, 7, 40566.
- 549 Chen, H.Y., Zhang, S.T., Chu, G.B., Zhang, Y., Cheng, J.M., Tian, J. and Han, J.S. (2019) The short wave
550 infrared (SWIR) spectral characteristics of alteration minerals and applications for ore exploration in

- 551 the typical skarn-porphyry deposits, Edong ore district, eastern China. *Acta Petrologica Sinica*, 35,
552 3629–3643 (in Chinese with English abstract).
- 553 Chiaradia, M. (2014) Copper enrichment in arc magmas controlled by overriding plate thickness. *Nature*
554 *Geoscience*, 7, 43–46.
- 555 Chiaradia, M., and Caricchi, L. (2017) Stochastic modelling of deep magmatic controls on porphyry copper
556 deposit endowment. *Scientific Reports*, 7, 44523.
- 557 Cline, J. S., and Bodnar, R. J. (1991) Can economic porphyry copper mineralization be generated by a
558 typical calc-alkaline melt? *Journal of Geophysical Research: Solid Earth*, 96, 8113–8126.
- 559 Cooke, D.R., Hollings, P., and Walshe, J.L. (2005) Giant porphyry deposits: Characteristics, distribution,
560 and tectonic controls. *Economic Geology*, 100, 801–818.
- 561 Davidson, J., Turner, S., and Plank, T. (2013) Dy/Dy^* : variations arising from mantle sources and
562 petrogenetic processes. *Journal of Petrology*, 54, 525–537.
- 563 Du J., and Audétat A. (2020) Early sulfide saturation is not detrimental to porphyry Cu-Au formation.
564 *Geology*, 48, 519–524.
- 565 Duan, D., and Jiang, S. (2017) In situ major and trace element analysis of amphiboles in quartz
566 monzodiorite porphyry from the Tonglvshan Cu–Fe (Au) deposit, Hubei Province, China: insights into
567 magma evolution and related mineralization. *Contributions to Mineralogy and Petrology*, 172, 36.
- 568 Evans, K., and Tomkins, A. G. (2011) The relationship between subduction zone redox budget and arc
569 magma fertility. *Earth and Planetary Science Letters*, 308, 401–409.
- 570 Halter, W.E., Pettke, T., and Heinrich, C.A. (2002) The origin of Cu/Au ratios in porphyry-type ore deposits.
571 *Science*, 296, 1844–1846.
- 572 Halter, W.E., Heinrich, C.A. and Pettke, T. (2004) Laser-ablation ICP-MS analysis of silicate and sulfide

- 573 melt inclusions in an andesitic complex II: evidence for magma mixing and magma chamber evolution.
574 Contributions to Mineralogy and Petrology, 147, 397–412.
- 575 Halter, W.E., Heinrich, C.A., and Pettke, T. (2005) Magma evolution and the formation of porphyry Cu-Au
576 ore fluids: evidence from silicate and sulfide melt inclusions. Mineralium Deposita, 39, 845–863.
- 577 Hao, H., Campbell, I.H., Park, J.-W., and Cooke, D.R. (2017) Platinum-group element geochemistry used
578 to determine Cu and Au fertility in the Northparkes igneous suites, New South Wales, Australia.
579 Geochimica et Cosmochimica Acta, 216, 372–392
- 580 Hedenquist, J. W., and Lowenstern, J. B. (1994) The role of magmas in the formation of hydrothermal ore
581 deposits. Nature, 370, 519–527.
- 582 Hedenquist, J. W., Arribas, A., and Reynolds, T. J. (1998) Evolution of an intrusion-centered hydrothermal
583 system; Far Southeast-Lepanto porphyry and epithermal Cu-Au deposits, Philippines. Economic
584 Geology, 93, 373–404.
- 585 Holland, H.D. (1972) Granites, solutions, and base metal deposits. Economic Geology, 67, 281–301.
- 586 Hou, Z.Q., Pan, X.F., Li, Q.Y., Yang, Z.M., and Song, Y.C. (2013) The giant Dexing porphyry Cu-Mo-Au
587 deposit in east China, product of melting of juvenile lower crust in an intracontinental setting.
588 Mineralium Deposita, 48, 1019–1045.
- 589 Hou, Z., Yang, Z., Lu, Y., Kemp, A. I., Zheng, Y., Li, Q., Tang, J., Yang, Z., and Duan, L. (2015) A genetic
590 linkage between subduction- and collision-related porphyry Cu deposits in continental collision zones.
591 Geology, 43, 247–250.
- 592 Hu, X., Chen, H., Zhao, L., Han, J., and Xia, X. (2017) Magnetite geochemistry of the Longqiao and
593 Tieshan Fe-(Cu) deposits in the Middle-Lower Yangtze River Belt: Implications for deposit type and
594 ore genesis. Ore Geology Reviews, 89, 822–835.

- 595 Ishihara, S. (1977) The magnetite-series and ilmenite-series granitic rocks. *Mining Geology*, 27, 293–305.
- 596 Ishihara, S. (1981) The granitoid series and mineralization. In Skinner, B. J. (ed.) *Economic Geology 75th*
597 anniversary volume. Economic Geology Publishing Co., El Paso, 458–484
- 598 Jenner, F. E., Oneill, H. S., Arculus, R. J., and Mavrogenes, J. (2010) The magnetite crisis in the evolution
599 of arc-related magmas and the initial concentration of Au, Ag and Cu. *Journal of Petrology*, 51,
600 2445–2464.
- 601 Jugo, P. J., Wilke, M., and Botcharnikov, R. E. (2010) Sulfur K-edge XANES analysis of natural and
602 synthetic basaltic glasses: Implications for S speciation and S content as function of oxygen fugacity.
603 *Geochimica et Cosmochimica Acta*, 74, 5926–5938.
- 604 Keith, J.D., Whitney, J.A., Hattori, K., Ballantyne, G.H., Christiansen, E.H., Barr, D.L., Cannan, T.M., and
605 Hook, C.J. (1997) The role of magmatic sulfides and mafic alkaline magmas in the Bingham and Tintic
606 mining districts, Utah. *Journal of Petrology*, 38, 1679–1690.
- 607 Kelley, K. A., and Cottrell, E. (2012) The influence of magmatic differentiation on the oxidation state of Fe
608 in a basaltic arc magma. *Earth and Planetary Science Letters*, 329–330, 109–121.
- 609 Kohn, M. J. (2017) Titanite Petrochronology: *Reviews in Mineralogy and Geochemistry*, 83, 419–441.
- 610 Larocque, A.C.L., Stimac, J.A., Keith, J.D., and Huminicki, M.A.E. (2000) Evidence for open-system
611 behavior in immiscible Fe-S-O liquids in silicate magmas: Implications for contributions of metals and
612 sulfur to ore-forming fluids. *Canadian Mineralogist*, 38, 1233–1249.
- 613 Lee, C. A., Luffi, P., Roux, V. L., Dasgupta, R., Albarede, F., and Leeman, W. P. (2010) The redox state of
614 arc mantle using Zn/Fe systematics: *Nature*, 468, 681–685.
- 615 Lee, C. A., Luffi, P., Chin, E. J., Bouchet, R. A., Dasgupta, R., Morton, D. M., Roux, V. L., Yin, Q., and Jin,
616 D. (2012) Copper Systematics in Arc Magmas and Implications for Crust-Mantle Differentiation.

- 617 Science, 336, 64–68.
- 618 Li, J.W., Zhao, X.F., Zhou, M.F., Vasconcelos, P., Ma, C.Q., Deng, X.D., de Souza, Z.S., Zhao, Y.X., and
619 Wu, G. (2008) Origin of the Tongshankou porphyry-skarn Cu–Mo deposit, eastern Yangtze craton,
620 Eastern China: eochemical, geochemical, and Sr–Nd–Hf isotopic constraints. *Mineralium Deposita*,
621 43, 315–336.
- 622 Li, J. W., Zhao, X. F., Zhou, M. F., Ma, C. Q., de Souza, Z. S., and Vasconcelos, P. (2009) Late Mesozoic
623 magmatism from the Daye region, eastern China: U–Pb ages, petrogenesis, and geodynamic
624 implications. *Contributions to Mineralogy and Petrology*, 157, 383–409.
- 625 Li, J.W., Vasconcelos, P.M., Zhou, M.F., Deng, X.D., Cohen, B., Bi, S.J., Zhao, X.F., and Selby, D. (2014)
626 Longevity of magmatic-hydrothermal systems in the Daye Cu-Fe-Au district, eastern China with
627 implications for mineral exploration. *Ore Geology Reviews*, 57, 375–392.
- 628 Li, X. H., Li, Z. X., Zhou, H. W., Liu, Y. and Kinny, P. D. (2002) U-Pb zircon geochronology, geochemistry
629 and Nd isotopic study of Neoprozoic bimodal volcanic rocks in the Kangdian Rift of south China:
630 implications for the initial rifting of Rodinia. *Precambrian Research*, 113, 135–154.
- 631 Li, Y., Selby, D., Condon, D., and Tapster, S. (2017) Cyclic magmatic-hydrothermal evolution in porphyry
632 systems: high-precision U-Pb and Re-Os geochronology constraints on the Tibetan Qulong porphyry
633 Cu-Mo deposit. *Economic Geology*, 112, 1419–1440.
- 634 Liu, J.S., Ma, G., and Shu, and G.L. (2005) Discovery of cryptoexplosive breccia type Cu (Au) orebodies in
635 Tonglushan skarn-type Cu-Fe deposit of Hubei Province and ore-searching vista. *Mineral Deposits*, 24,
636 527–534 (in Chinese with English abstract).
- 637 Meinert, L. D., Hedenquist, J. W., Satoh, H., and Matsuhisa, Y. (2003) Formation of Anhydrous and
638 Hydrous Skarn in Cu-Au Ore Deposits by Magmatic Fluids. *Economic Geology*, 98, 147–156.

- 639 Meinert, L.D., Dipple, G.M., and Nicolescu, S. (2005) World skarn deposits. *Economic Geology* 100th
640 Anniversary Volume, 299–336.
- 641 Mercer, C. N., Reed, M. H., and Mercer, C. M. (2015) Time Scales of Porphyry Cu Deposit Formation:
642 Insights from Titanium Diffusion in Quartz. *Economic Geology*, 110, 587–602.
- 643 Mungall, J. E. (2002) Roasting the mantle: Slab melting and the genesis of major Au and Au-rich Cu
644 deposits. *Geology*, 30, 915–918.
- 645 Nadeau, O., Williams-Jones, A.E., and Stix, J. (2010) Sulphide magma as a source of metals in arc-related
646 magmatic hydrothermal ore fluids. *Nature Geoscience*, 3, 501–505.
- 647 Nadeau, O., Stix, J., and Williams-Jones, A.E. (2013) The behavior of Cu, Zn and Pb during
648 magmatic–hydrothermal activity at Merapi volcano, Indonesia. *Chemical Geology*, 342, 167–179.
- 649 O'Neill, H. S. C., and Pownceby, M. I. (1993) Thermodynamic data from redox reactions at high
650 temperatures. I. An experimental and theoretical assessment of the electrochemical method using
651 stabilized zirconia electrolytes, with revised values for the Fe–“FeO”, Co–CoO, Ni–NiO and Cu–Cu₂O
652 oxygen buffers, and new data for the W–WO₂ buffer. *Contributions to Mineralogy and Petrology*, 114,
653 296–314.
- 654 Park, J.-W., Campbell, I.H., Kim, J., and Moon, J.-W. (2015) The role of late sulfide saturation in the
655 formation of a Cu- and Au-rich magma: Insights from the platinum-group geochemistry of
656 Niuatahi-Motutahi lavas, Tonga rear arc. *Journal of Petrology*, 56, 59–81.
- 657 Park, J.-W., Campbell, I.H., Malaviarachchi, S.P.K., Cocker, H., Hao, H., and Kay, S.M. (2019)
658 Chalcophile element fertility and the formation of porphyry Cu ± Au deposits. *Mineralium Deposita*, 54,
659 657–670.
- 660 Paterson, B. A., and Stephens, W. E. (1992) Kinetically induced compositional zoning in titanite:

- 661 implications for accessory-phase/melt partitioning of trace elements. *Contributions to Mineralogy and*
662 *Petrology*, 109, 373–385.
- 663 Piccoli, P. M., Candela, P. A., and Rivers, M. L. (2000) Interpreting magmatic processes from accessory
664 phases: titanite—a small-scale recorder of large-scale processes. *Transactions of The Royal Society of*
665 *Edinburgh-earth Sciences*, 91, 257–267.
- 666 Pirajno, F. and Zhou, T. (2015) Intracontinental porphyry and porphyry-skarn mineral systems in eastern
667 china: scrutiny of a special case "made-in-China". *Economic Geology*, 110, 603–629.
- 668 Putirka, K. (2016) Amphibole thermometers and barometers for igneous systems and some implications for
669 eruption mechanisms of felsic magmas at arc volcanoes. *American Mineralogist*, 101, 841–858.
- 670 Richards, J. P. (2003) Tectono-magmatic precursors for porphyry Cu-(Mo-Au) deposit formation.
671 *Economic Geology*, 98, 1515–1533.
- 672 Richards, J. P. (2013) Giant ore deposits formed by optimal alignments and combinations of geological
673 processes. *Nature Geoscience*, 6, 911–916.
- 674 Richards, J. P. (2015) The oxidation state, and sulfur and Cu contents of arc magmas: implications for
675 metallogeny. *Lithos*, 233, 27–45.
- 676 Ridolfi, F., Renzulli, A., and Puerini, M. (2010) Stability and chemical equilibrium of amphibole in
677 calc-alkaline magmas: an overview, new thermobarometric formulations and application to
678 subduction-related volcanoes. *Contributions to Mineralogy and Petrology*, 160, 45–66.
- 679 Seedorff, E., Dilles, J. H., Proffett, J. M., Einaudi, M. T., Zurcher, L., Stavast, W. J. A., Johnson, D. A. and
680 Barton, M. D. (2005) Porphyry deposits: characteristics and origin of hypogene features. *Economic*
681 *Geology 100th Anniversary Volume*, 29, 251–298.
- 682 Seo, J. H., Guillong, M., and Heinrich, C. A. (2009) The role of sulfur in the formation of

- 683 magmatic–hydrothermal copper–gold deposits. *Earth and Planetary Science Letters*, 282, 323–328.
- 684 Shu, Q.A., Chen, P.R., and Chen, J.R. (1992) *Geology of Fe–Cu Ore Deposits in Eastern Hubei Province*,
685 1st ed. Press of Metallurgical Industry, Beijing.
- 686 Sillitoe, R. H. (2010) Porphyry copper systems. *Economic geology*, 105, 3–41.
- 687 Sillitoe, R. H. (2012) Copper provinces, in Hedenquist, J. W., Harris, M. and Camus F., ed., *Geology and*
688 *Genesis of Major Copper Deposits and Districts of the world: A Tribute to Richard H. Sillitoe*. Society
689 of Economic Geologists, Special Publication 16, 1–18.
- 690 Sillitoe, R. H. (2018) Why no porphyry copper deposits in Japan and South Korea? *Resource Geology*, 68,
691 107–125.
- 692 Simmons, S. F., White, N. C. and John, D. A. (2005) Geological characteristics of epithermal precious and
693 base metal deposits. *Economic Geology 100th Anniversary Volume*, 485–522.
- 694 Simon, A. C., Pettke, T., Candela, P. A., Piccoli, P. M., and Heinrich, C. A. (2004) Magnetite solubility and
695 iron transport in magmatic-hydrothermal environments. *Geochimica et Cosmochimica Acta*, 68,
696 4905–4914.
- 697 Song, S., Mao, J., Xie, G., Chen, L., Santosh, M., Chen, G., Rao, J., and Ouyang, Y. (2019) In situ
698 LA-ICP-MS U–Pb geochronology and trace element analysis of hydrothermal titanite from the giant
699 Zhuxi W (Cu) skarn deposit, South China. *Mineralium Deposita*, 54, 569–590.
- 700 Spooner, E.T.C. (1993) Magmatic sulphide/volatile interaction as a mechanism for producing chalcophile
701 element enriched, Archean Au-quartz, epithermal Au-Ag and Au skarn hydrothermal ore fluids. *Ore*
702 *Geology Reviews*, 7, 359–379.
- 703 Stavast, W.J.A., Keith, J.D., Christiansen, E.H., Dorais, M.J. and Tingey, D. (2006) The fate of magmatic
704 sulfides during intrusion or eruption, Bingham and Tintic districts, Utah. *Economic Geology*, 101,

705 329–345.

706 Tattitch, B., and Blundy, J. D. (2017) Cu-Mo partitioning between felsic melts and saline-aqueous fluids as
707 a function of $X_{\text{NaCl}_{\text{aq}}}$, f_{O_2} , and f_{S_2} . *American Mineralogist*, 102, 1987–2006.

708 Tattitch, B., Chelle-Michou, C., Blundy, J., and Loucks, R. R. (2021) Chemical feedbacks during magma
709 degassing control chlorine partitioning and metal extraction in volcanic arcs. *Nature communications*,
710 12, 1–11.

711 Wang, Q., Zhao, Z.H., Bao, Z.W., Xu, J.F., Liu, W., Li, C.F., Bai, Z.H., and Xiong, X. L. (2004)
712 Geochemistry and petrogenesis of the Tongshankou and Yinzu adakitic intrusive rocks and the
713 associated porphyry copper-molybdenum mineralization in southeast Hubei, east China. *Resource*
714 *Geology*, 54, 137–152.

715 Wang Q., Xu J. F., Jian P., Bao Z. W., Zhao Z. H., Li C. F., Xiong X. L., and Ma J. L. (2006) Petrogenesis
716 of adakitic porphyries in an extensional tectonic setting, Dexing, South China: implications for the
717 genesis of porphyry copper mineralization. *Journal of Petrology*, 47, 119–144.

718 Wang, R., Richards, J. P., Hou, Z., Yang, Z., and DuFrane, S. A. (2014) Increased magmatic water
719 content—the key to Oligo-Miocene porphyry Cu-Mo±Au formation in the eastern Gangdese belt, Tibet.
720 *Economic Geology*, 109, 1315–1339.

721 Watson, E. B., and Liang, Y. (1995) A simple model for sector zoning in slowly grown crystals;
722 implications for growth rate and lattice diffusion, with emphasis on accessory minerals in crustal rocks.
723 *American Mineralogist*, 80, 1179–1187.

724 Wilkinson, J. J. (2013) Triggers for the formation of porphyry ore deposits in magmatic arcs. *Nature*
725 *Geoscience*, 6, 917–925.

726 Williams-Jones, A.E., and Heinrich, C.A. (2005) Vapor transport of metals and the formation of

- 727 magmatic-hydrothermal ore deposits. *Economic Geology* 100th Anniversary Volume, 1287–1312.
- 728 Williamson, B. J., Herrington, R. J., and Morris, A. (2016) Porphyry copper enrichment linked to excess
729 aluminium in plagioclase. *Nature Geoscience*, 9, 237–241.
- 730 Xie, G.Q., Mao, J.W., Li, R.L., Qu, W.J., Pirajno, F., and Du, A.D. (2007) Re–Os molybdenite and Ar–Ar
731 phlogopite dating of Cu–Fe–Au–Mo (W) deposits in southeastern Hubei, China. *Mineralogy and*
732 *Petrology*, 90, 249–270.
- 733 Xie, G., Mao, J., and Zhao, H. (2011) Zircon U–Pb geochronological and Hf isotopic constraints on
734 petrogenesis of Late Mesozoic intrusions in the southeast Hubei Province, Middle–Lower Yangtze
735 River belt (MLYRB), East China. *Lithos*, 125, 693–710.
- 736 Yang, Z., Lu, Y., Hou, Z., and Chang, Z. (2015) High-Mg diorite from Qulong in southern Tibet:
737 Implications for the genesis of adakite-like intrusions and associated porphyry Cu deposits in collisional
738 orogens. *Journal of Petrology*, 56, 227–254.
- 739 Yu, Y.C., Li, G., Xiao, G.Q., Yang, H.C., Xue, D.K., Liu, Y.L., and Li, J.Z. (1985) The Tonglushan Cu–Fe
740 Skarn Deposit. Geological Team of Southeast Hubei Province, Daye.
- 741 Zajacz, Z., and Halter, W. E. (2009) Copper transport by high temperature, sulfur-rich magmatic vapor:
742 Evidence from silicate melt and vapor inclusions in a basaltic andesite from the Villarrica volcano
743 (Chile). *Earth and Planetary Science Letters*, 282, 115–121.
- 744 Zajacz, Z., Halter, W. E., Pettke, T., and Guillong, M. (2008) Determination of fluid/melt partition
745 coefficients by LA-ICPMS analysis of co-existing fluid and silicate melt inclusions: Controls on
746 element partitioning. *Geochimica et Cosmochimica Acta*, 72, 2169–2197.
- 747 Zajacz, Z., Seo, J. H., Candela, P. A., Piccoli, P. M., and Tossell, J. A. (2011) The solubility of copper in
748 high-temperature magmatic vapors: A quest for the significance of various chloride and sulfide

- 749 complexes. *Geochimica et Cosmochimica Acta*, 75, 2811–2827.
- 750 Zajacz, Z., Candela, P. A., Piccoli, P. M., Walle, M., and Sanchezvalle, C. (2012) Gold and copper in
751 volatile saturated mafic to intermediate magmas: Solubilities, partitioning, and implications for ore
752 deposit formation. *Geochimica et Cosmochimica Acta*, 91, 140–159.
- 753 Zhang, D., and Audetat, A. (2017) What Caused the Formation of the Giant Bingham Canyon Porphyry
754 Cu-Mo-Au Deposit? Insights from Melt Inclusions and Magmatic Sulfides. *Economic Geology*, 112,
755 221–244.
- 756 Zhang, D., and Audetat, A. (2018) Magmatic-hydrothermal evolution of the barren Huangshan Pluton,
757 Anhui Province, China: A melt and fluid inclusion study. *Economic Geology*, 113, 803–824.
- 758 Zhang, L., Ren, Z. Y., Xia, X. P., Yang, Q., Hong, L. B., and Wu, D. (2019) In situ determination of trace
759 elements in melt inclusions using laser ablation inductively coupled plasma sector field mass
760 spectrometry. *Rapid Communications in Mass Spectrometry*, 33, 361–370.
- 761 Zhao, H., Xie, G., Wei, K., and Ke, Y. (2012) Mineral compositions and fluid evolution of the Tonglushan
762 skarn Cu–Fe deposit, SE Hubei, East-Central China. *International Geology Review*, 54, 737–764.
- 763 Zheng Y. C., Liu S. A., Wu C. D., Griffin W. L., Li Z. Q., Xu B., Yang Z. M., Hou Z. Q. and O’Reilly S. Y.
764 (2019) Cu isotopes reveal initial Cu enrichment in sources of giant porphyry deposits in a collisional
765 setting. *Geology*, 47, 135–138.
- 766 Zhou J.-S., Wang Q., Wyman D. A., and Zhao Z.-H. (2020a) Petrologic reconstruction of the Tieshan
767 magma plumbing system: Implications for the genesis of magmatic-hydrothermal ore deposits within
768 originally water-poor magmatic systems: *Journal of Petrology*, ega056.
- 769 Zhou, J.-S., Yang Z.-S., Hou, Z.-Q., and Wang, Q. (2020b) Amphibole-rich cumulate xenoliths in the
770 Zhazhalong intrusive suite, Gangdese arc: Implications for the role of amphibole fractionation during

- 771 magma evolution. *American Mineralogist*, 105, 262–275.
- 772 Zhou, J.-S., Wang, Q., Xing, C.-M., Ma, L., Hao, L.-L., Li, Q.-W., Wang, Z.-L., and Huang, T.-Y. (2021)
- 773 Crystal growth of clinopyroxene in mafic alkaline magmas. *Earth and Planetary Science Letters*, 568,
- 774 117005.
- 775 Zhou, T., Wang, S., Fan, Y., Yuan, F., Zhang, D. and White, N. C. (2015) A review of the intracontinental
- 776 porphyry deposits in the Middle-Lower Yangtze River Valley metallogenic belt, Eastern China. *Ore*
- 777 *Geology Reviews*, 65, 433–456.
- 778 Zhu, Q., Xie, G., Mao, J., Li, W., Li, Y., Wang, J., and Zhang, P. (2015) Mineralogical and sulfur isotopic
- 779 evidence for the incursion of evaporites in the Jinshandian skarn Fe deposit, Edong district, Eastern
- 780 China. *Journal of Asian Earth Sciences*, 113, 1253–1267.
- 781 Zhu, Q., Xie, G., Mao, J., Hou, K., Sun, J., and Jiang, Z. (2017) Formation of the Jinshandian Fe skarn ore
- 782 field in the Edong district, Eastern China: Constraints from U–Pb and $^{40}\text{Ar}/^{39}\text{Ar}$ geochronology. *Ore*
- 783 *Geology Reviews*, 86, 1–20.

784

785 **Figure captions**

786 **Fig. 1.** Simplified geological map showing the distribution of Cretaceous intrusions, volcanics and

787 magmatic-hydrothermal ore deposits in the Edong District. Modified from Xie et al. (2011) and Li et al.

788 (2014). The inset map shows regional-scale characteristics and the location of the Edong District (modified

789 from Li et al., 2009).

790 **Fig. 2.** (A) Geologic map of the Tieshan Fe-Cu deposit (from Zhu et al., 2019); (B) Geologic map of

791 the Jinshandian Fe deposit (modified from Zhu et al., 2017); (C) Geologic map of the Tonglushan Fe

792 deposit (from Li et al., 2014).

793 **Fig. 3.** Photographs of titanites from the three plutons. (A) Magmatic titanite and apatite grains in the
794 Tonglushan pluton; (B) Magmatic titanite in the Tonglushan pluton; (C) Euhedral amphibole in the Tieshan
795 pluton; (D) Anhedral amphibole in the Tieshan pluton; (E) Magmatic titanite in the Jinshandian pluton; (F)
796 Secondary titanite with Fe-Ti oxide inclusions with irregular shapes in the Jinshandian pluton. Mineral
797 abbreviations: Ttn = titanite, Ap = apatite, Amp = amphibole, Pl = plagioclase, Qz = quartz, Mag =
798 magnetite.

799 **Fig. 4.** (A) Plot of SiO₂ contents in equilibrium with amphiboles versus temperatures. Equations 5
800 and 10 from Putirka (2016) were employed to estimate temperature and equilibrium melt SiO₂ contents.; (B)
801 Magmatic water contents versus temperatures. Equation 3 of Ridolfi *et al.* (2010) was used to calculate
802 water content, and Equation 5 of Putirka (2016) was employed to estimate temperature; (C) and (D)
803 Magmatic oxygen fugacities versus temperatures. Equation 2 of Ridolfi *et al.* (2010) was used to calculate
804 oxygen fugacity, and Equation 5 of Putirka (2016) was employed to estimate temperature. The calibrations
805 of the nickel-nickel oxide (NNO) buffer is taken from O'Neill & Pownceby (1993).

806 **Fig. 5.** BSE and X-ray mapping images of two euhedral, magmatic titanite crystals with sector zoning.
807 They are from the Tonglushan pluton. Cu and Ce concentrations are marked in different sectors of crystal
808 (B).

809 **Fig. 6.** Box-whisker plots of mineral Cu concentrations for the Tonglushan, Tieshan, and Jinshandian
810 plutons. Number of analyses is marked above each box plot. The top and bottom of the boxes are the first
811 and second quartiles. The black line is the median, and the full circle is the average. The whiskers represent
812 the values within 1.5 times the interquartile range beyond the box edges. The full rhombuses represent
813 outliers.
814

815 **Table caption**

816 **Table 1.** Representative whole-rock major and trace element compositions of the Tonglushan, Tieshan,
817 and Jinshandian plutonic rocks

818 **Table 2.** Representative clinopyroxene major and trace element compositions

819 **Table 3.** Representative feldspar major and trace element compositions

820 **Table 4.** Representative amphibole major and trace element compositions

821 **Table 5.** Representative titanite major and trace element compositions

822 **Table 6.** Representative apatite major and trace element compositions

823 **Table 7.** Comparison of the Tonglushan, Tieshan, and Jinshandian plutons

824

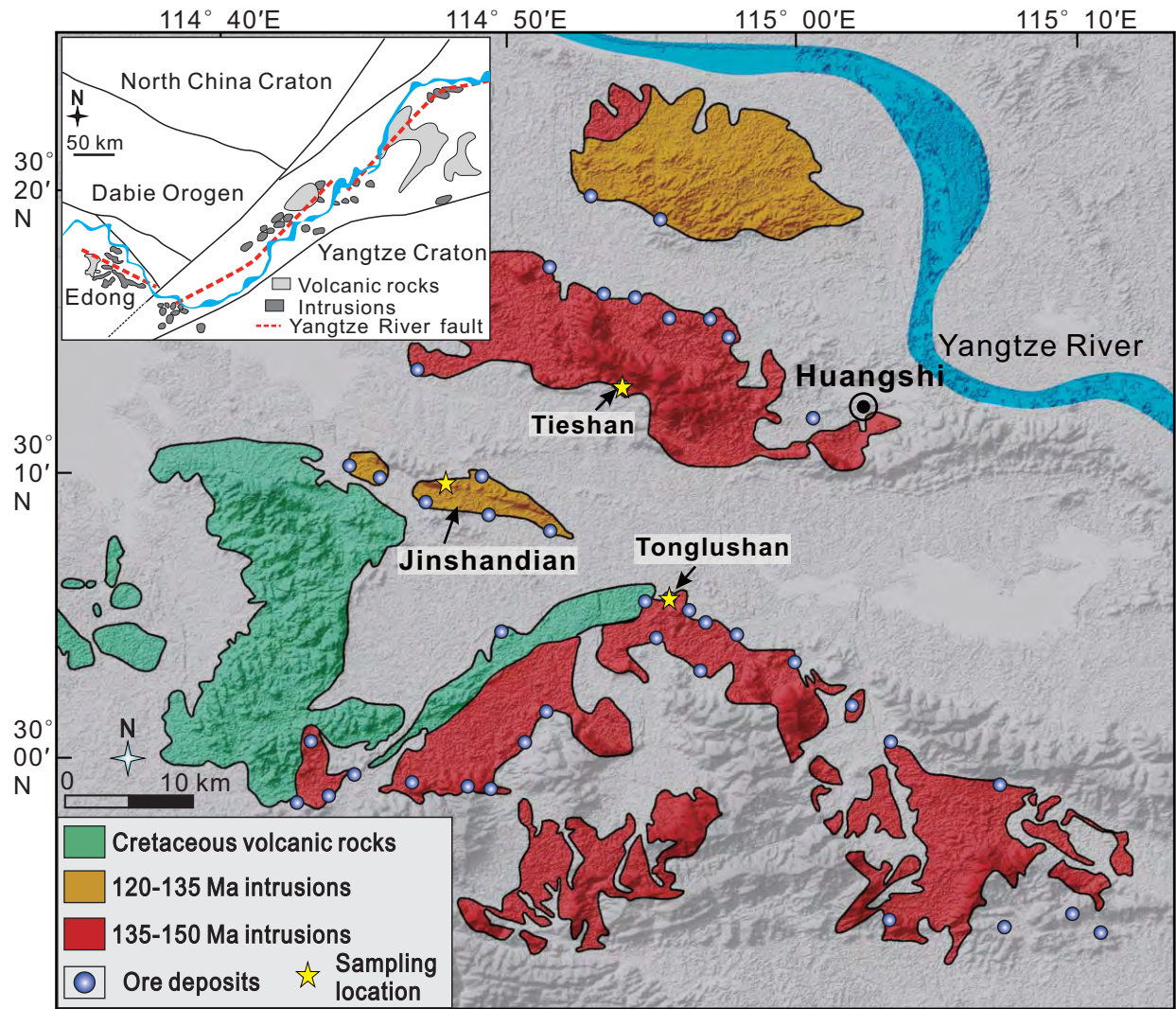


Figure 1

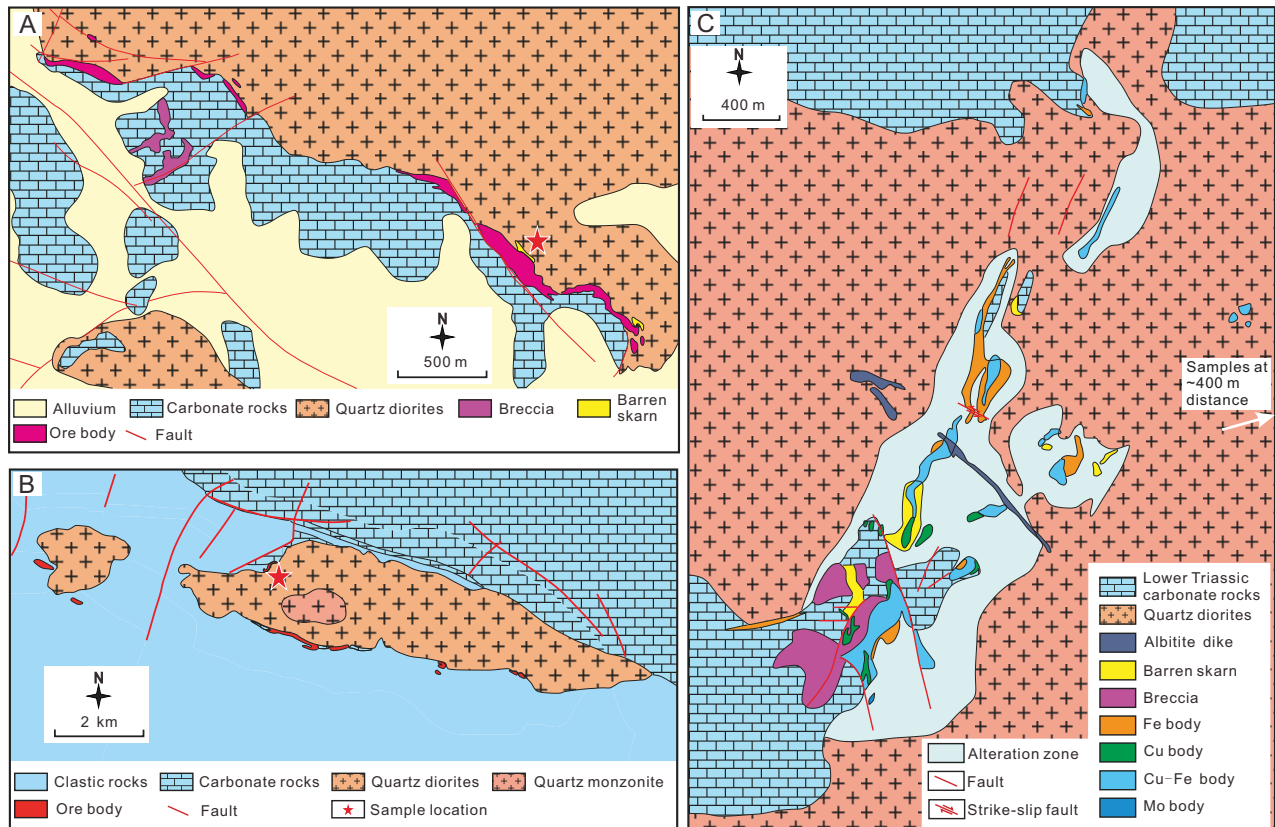


Figure 2

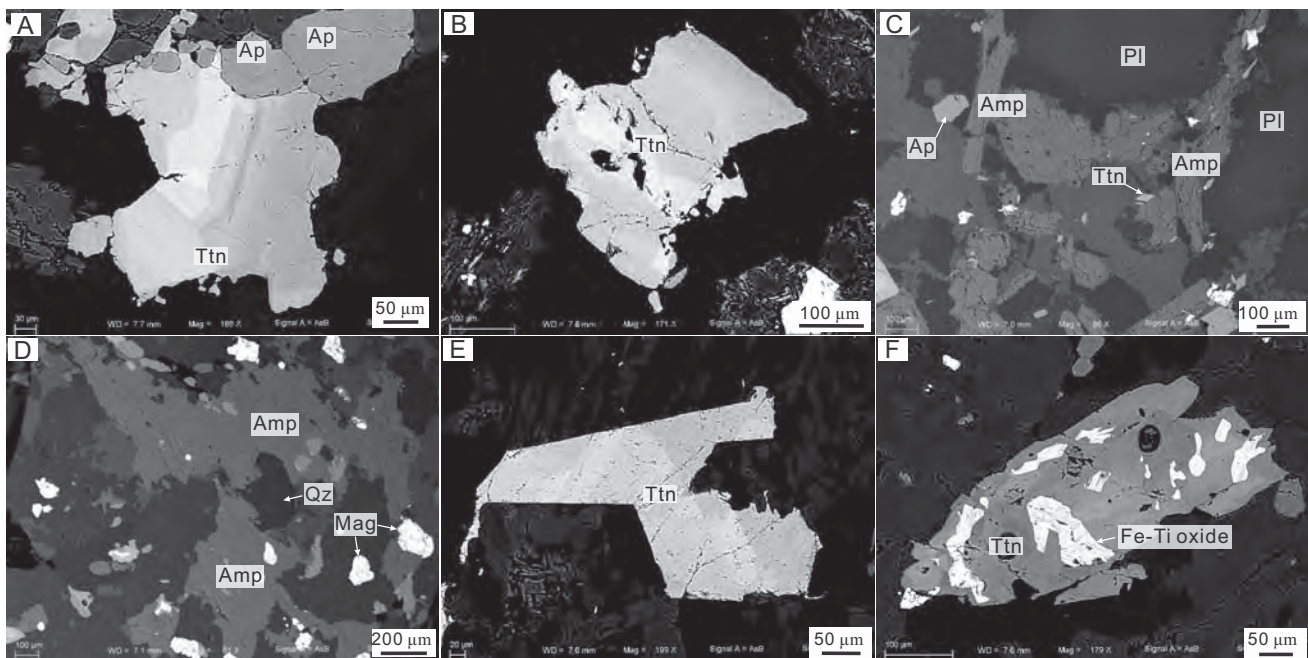


Figure 3

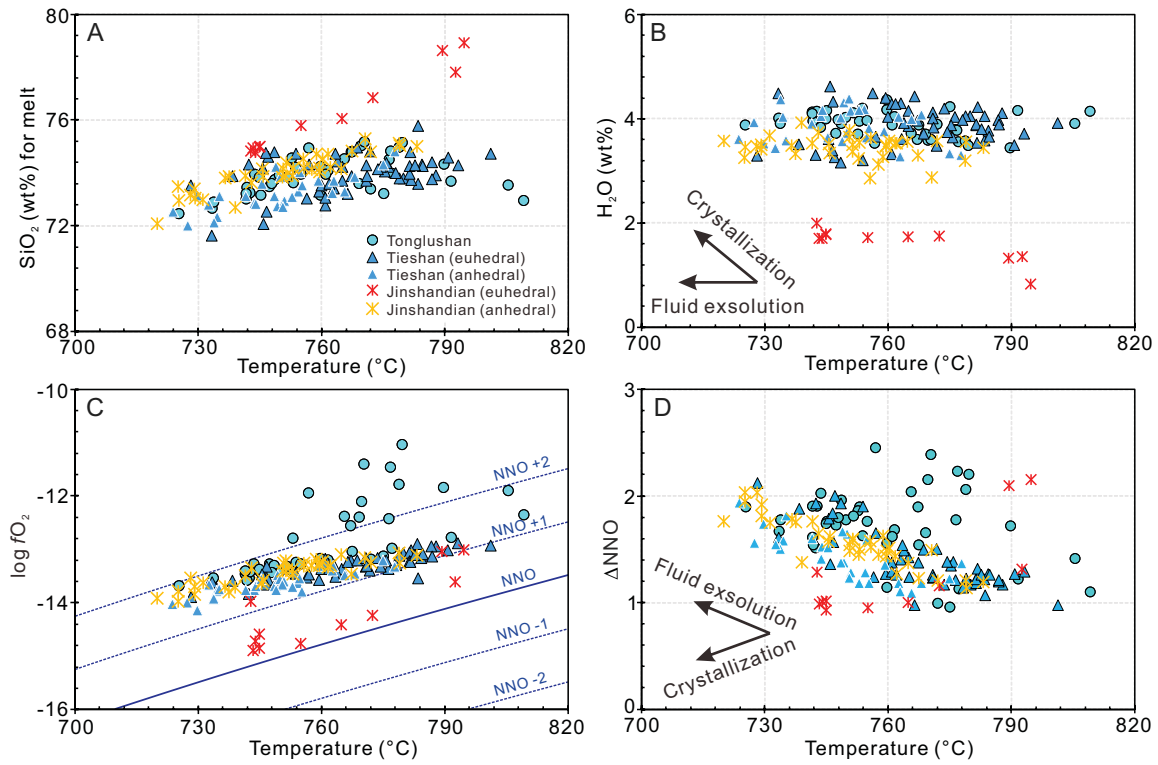


Figure 4

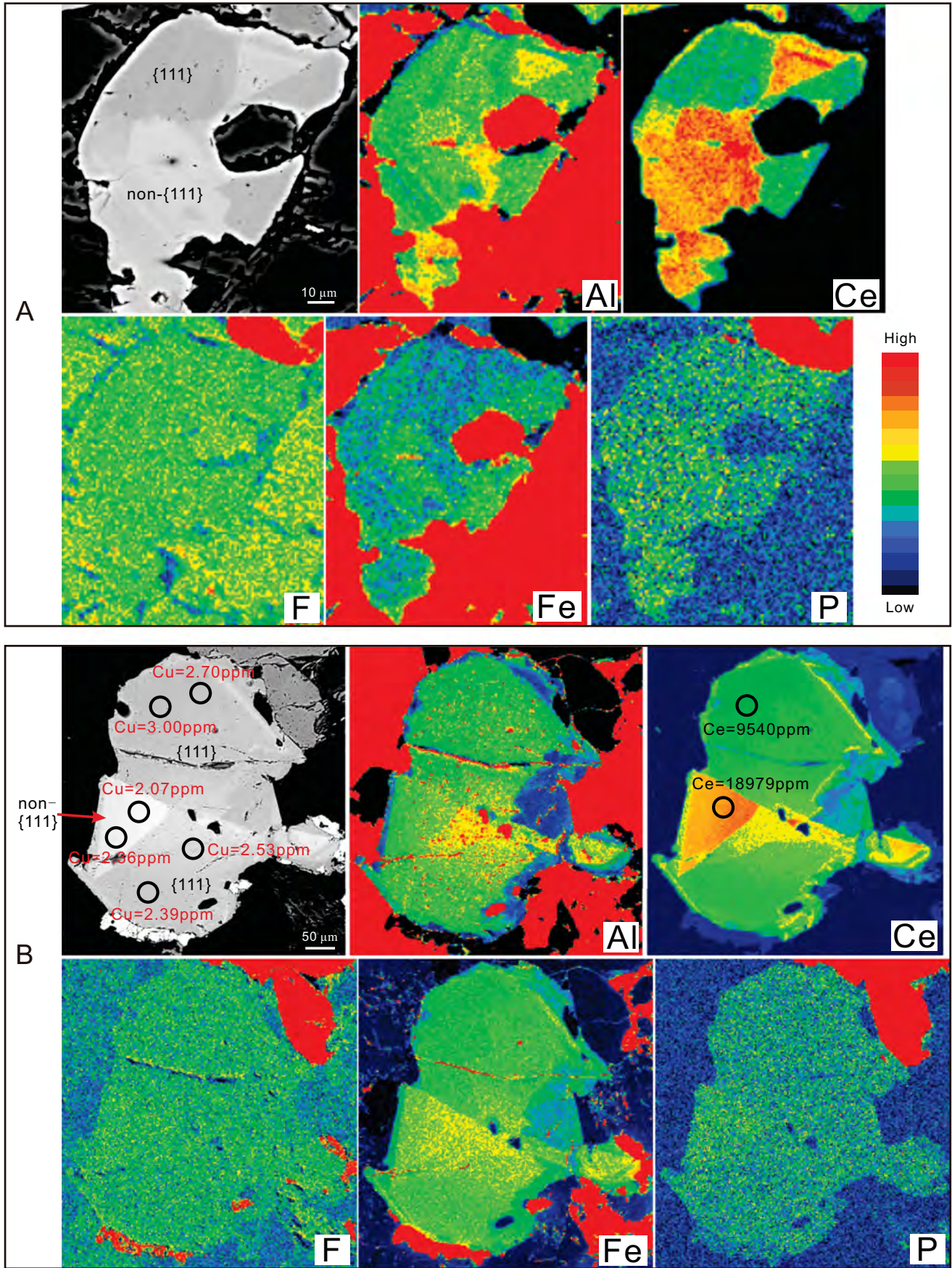


Figure 5

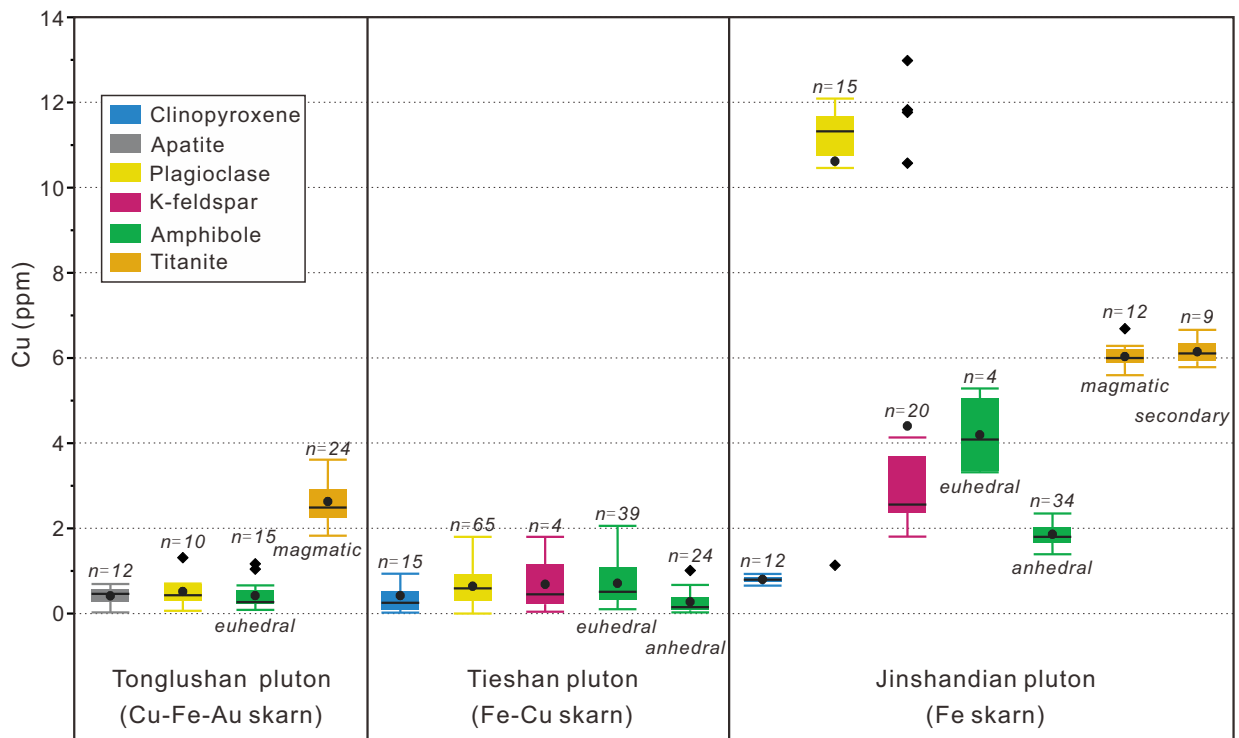


Figure 6

Table 1. Representative whole-rock major and trace element compositions of the Tonglushan, Tieshan, and Jinshandi:

Sample:	HB-008	HB-009	HB001	HB003	HB006	HB007	ts1	ts4
Deposit	Tonglushan Cu-Fe-Au skarn deposit		Tieshan Fe-Cu skarn deposit					
Lithology	Quartz monzodiorite		Quartz diorite					
Major oxides(wt%)								
SiO ₂	63.68	62.64	63.77	64.73	64.19	62.84	63.12	62.82
TiO ₂	0.55	0.56	0.54	0.57	0.50	0.56	0.67	0.65
Al ₂ O ₃	15.92	16.17	15.81	15.76	15.98	16.47	16.15	16.18
TFe ₂ O ₃	4.89	4.86	4.30	4.32	4.28	4.18	4.83	4.82
MnO	0.08	0.09	0.05	0.06	0.07	0.05	0.07	0.07
MgO	1.44	0.86	1.62	1.68	1.42	1.88	1.81	1.88
CaO	4.98	5.55	3.99	3.68	4.21	3.94	4.20	4.29
Na ₂ O	4.35	4.53	4.84	5.02	5.57	5.60	5.07	5.07
K ₂ O	2.75	2.71	3.30	2.97	2.67	3.06	2.98	3.17
P ₂ O ₅	0.26	0.26	0.24	0.24	0.23	0.29	0.29	0.29
LOI	1.06	1.73	1.32	0.83	0.73	0.75	0.67	0.59
Total	99.73	99.73	99.53	99.65	99.63	99.43	99.62	99.60
Trace elements (ppm)								
Cr	6.98	6.65	25.7	25.2	12.9	22.7	19.1	19.2
Ni	5.83	6.52	14.46	15.74	8.01	18.5	14.0	14.9
Co	9.45	9.29	7.93	10.5	8.75	10.5	10.5	10.6
Sc	6.35	5.38	4.98	5.95	5.62	6.29	6.70	6.42
V	70.9	68.6	69.0	63.4	60.1	70.6	69.7	71.0
Pb	8.78	8.53	23.62	11.22	10.75	8.85	9.19	9.62
Rb	93.1	89.3	85.0	72.6	57.3	53.8	95.2	63.9
Cs	1.06	1.11	1.81	1.27	0.56	0.35	0.99	0.57
Ba	734	692	1016	985	1210	2238	1157	1245
Sr	961	983	1609	1433	1786	2100	1467	1531
Ga	22.3	21.2	24.1	24.5	24.0	23.6	23.9	24.2
Ta	1.03	1.08	0.75	0.78	0.80	0.72	0.86	0.82
Nb	18.1	18.0	13.4	14.2	15.0	13.8	14.3	14.0
Hf	4.04	4.19	5.07	5.28	3.56	2.73	5.23	5.17
Zr	131	131	166	168	121	79	187	184
Y	17.0	18.3	13.3	13.8	15.0	14.3	16.3	15.9
Th	13.4	13.1	7.5	8.3	6.4	7.7	10.1	9.9
U	3.24	2.94	2.24	2.35	1.73	1.44	2.24	2.21
La	51.0	51.0	42.6	46.6	53.4	58.7	59.6	61.7
Ce	97.7	96.5	84.8	90.1	105	118	113	116
Pr	10.3	10.0	9.32	9.82	11.4	13.0	13.3	13.6
Nd	37.8	38.2	35.4	36.6	42.2	50.4	50.0	51.3
Sm	6.83	6.94	6.41	6.91	7.76	8.33	7.64	7.67
Eu	1.78	1.78	1.73	1.71	1.91	2.16	1.90	1.92
Gd	4.93	5.03	4.40	4.50	5.08	5.59	4.39	4.37
Tb	0.63	0.62	0.55	0.58	0.66	0.64	0.64	0.61
Dy	3.34	3.43	2.85	2.86	3.12	2.94	3.36	3.31
Ho	0.63	0.69	0.49	0.49	0.56	0.54	0.60	0.58
Er	1.88	2.07	1.29	1.46	1.50	1.47	1.61	1.56
Tm	0.25	0.28	0.18	0.18	0.22	0.20	0.22	0.22
Yb	1.71	1.66	1.09	1.20	1.20	1.23	1.40	1.41

Lu	0.24	0.24	0.15	0.16	0.21	0.15	0.23	0.22
Sr/Y	56.4	53.8	121	104	119	147	90.1	96.5
Eu/Eu*	0.94	0.92	0.99	0.94	0.93	0.97	1.00	1.01
Dy/Dy*	0.52	0.54	0.64	0.59	0.61	0.55	0.57	0.56
(La/Yb)_N	21.1	21.7	27.6	27.6	31.6	33.9	30.2	31.1
Data source	Zhou et al. (2020a)		Zhou et al. (2020a)					

Notes: LOI is loss on ignition.

an plutonic rocks				
JSD-1	JSD-2	JSD-3	JSD-6	JSD-8
Jinshandian Fe skarn deposit				
Quartz diorite				
68.24	66.57	58.08	66.38	69.65
0.65	0.69	0.86	0.85	0.50
15.11	15.50	14.59	15.77	14.34
1.71	1.91	9.78	1.89	3.15
0.02	0.03	0.04	0.03	0.04
1.11	1.05	1.35	1.10	0.90
2.43	2.95	3.67	3.29	1.02
6.86	7.44	4.13	7.61	4.44
1.64	1.21	2.87	1.41	4.91
0.15	0.16	0.20	0.23	0.14
2.00	2.44	4.91	1.34	0.84
99.92	99.95	100.48	99.90	99.93
2.80	2.95	1.60	1.89	2.92
2.34	1.82	2.17	1.52	2.04
2.49	2.03	5.15	3.43	2.42
5.38	6.01	6.10	5.17	4.26
26.8	26.6	43.9	48.2	32.5
3.51	2.61	2.22	4.18	6.12
33.4	25.9	75.4	32.4	182
0.27	0.11	0.93	0.49	0.65
671	544	815	775	879
277	180	190	207	266
19.5	20.0	18.2	20.2	17.8
2.26	2.10	1.95	2.28	2.16
29.5	28.4	30.1	34.5	22.3
8.45	10.67	7.41	9.47	6.34
305	415	273	367	227
29.7	30.4	21.4	36.2	20.4
21.0	19.3	15.2	18.6	23.5
3.23	3.12	2.39	3.13	5.52
43.5	49.5	75.4	64.1	35.4
93.9	103	126	136	69.5
11.1	11.8	13.3	16.2	7.95
39.6	41.1	44.9	57.1	28.0
6.69	6.71	6.59	8.99	4.55
1.38	1.32	1.20	1.87	0.85
5.35	5.16	4.21	6.57	3.37
0.91	0.91	0.74	1.15	0.59
5.36	5.52	4.07	6.80	3.61
1.08	1.11	0.77	1.33	0.73
3.11	3.23	2.06	3.78	2.16
0.49	0.50	0.29	0.59	0.34
3.26	3.42	1.86	3.76	2.31

0.53	0.56	0.30	0.60	0.38
9.33	5.92	8.88	5.73	13.1
0.70	0.68	0.69	0.75	0.66
0.56	0.54	0.53	0.57	0.51
9.47	10.3	28.7	12.1	10.8
This study				

Table 2. Representative clinopyroxene major and trace element compositions

Pluton		Tieshan							Jinshandian				
Sample		TS-1							JSD-2				
Spot	100	101	103	104	107	118	119	38	40	41	45	49	
Oxide contents (wt %)													
SiO ₂	54.00	53.48	53.58	53.76	53.53	53.61	53.99	53.24	52.43	52.60	52.77	52.06	
TiO ₂	0.14	0.16	0.06	0.09	0.10	0.14	0.11	0.20	0.11	0.09	0.13	0.39	
Al ₂ O ₃	0.63	0.55	0.48	0.47	0.49	0.58	0.45	0.76	0.90	0.61	0.57	1.40	
FeO	8.40	8.51	8.68	8.64	8.72	8.81	8.59	8.49	8.25	8.35	8.32	8.80	
MnO	0.57	0.54	0.60	0.66	0.55	0.60	0.63	0.29	0.23	0.27	0.29	0.23	
MgO	13.07	13.17	12.73	12.73	12.71	12.50	12.93	13.16	13.36	13.11	14.07	12.82	
CaO	22.72	22.72	22.55	22.68	22.88	23.16	22.80	24.09	24.17	24.75	23.21	23.82	
Na ₂ O	0.43	0.39	0.54	0.60	0.50	0.55	0.54	0.46	0.61	0.52	0.54	0.72	
K ₂ O	b.d.l.	b.d.l.	b.d.l.	b.d.l.	b.d.l.	0.01	0.00	0.01	b.d.l.	b.d.l.	0.01	0.01	
P ₂ O ₅	0.00	0.00	0.04	0.02	0.06	0.03	0.01	0.01	0.02	0.03	0.03	0.00	
Cr ₂ O ₃	0.00	0.01	b.d.l.	0.04	0.00	b.d.l.	0.04	b.d.l.	0.01	0.02	0.05	b.d.l.	
F	b.d.l.	b.d.l.	b.d.l.	b.d.l.	b.d.l.	b.d.l.	b.d.l.	b.d.l.	b.d.l.	b.d.l.	b.d.l.	b.d.l.	
Cl	0.01	0.01	0.02	b.d.l.	0.00	0.00	b.d.l.	0.01	0.00	b.d.l.	0.01	0.00	
Total	99.96	99.53	99.26	99.70	99.54	99.98	100.08	100.71	100.08	100.34	100.00	100.24	
Trace element contents (ppm)													
Cu	0.53	0.07	0.65	0.02	0.10	0.48	0.51	0.77	0.76	0.65	0.74	0.85	
Zn	166	171	210	167	172	166	175	145	132	142	172	144	
Pb	0.73	0.63	3.41	0.66	0.64	0.60	1.78	0.98	1.46	0.61	1.96	0.62	
P	12.6	6.27	9.24	5.65	18.71	10.9	10.7	11.3	6.56	10.2	8.09	11.4	
Li	53.0	55.3	57.7	55.4	62.6	64.5	62.1	57.9	49.1	48.0	65.8	59.2	
Sc	101	87.4	90.9	108.0	88.5	92.9	96.6	78.1	72.5	81.4	47.7	87.5	
V	95.6	98.7	131	93.2	130	94.6	116	150	152	156	116	183	
Cr	12.9	16.1	31.6	26.9	38.8	15.4	24.4	62.9	51.1	68.4	54.6	81.4	
Co	38.2	42.8	42.0	44.2	42.3	42.3	40.3	35.7	35.2	35.3	43.3	38.8	
Ni	23.8	28.4	25.5	30.2	23.5	30.0	21.6	55.0	44.7	46.9	63.4	48.7	
Ga	7.38	8.18	12.3	7.12	10.4	7.64	8.85	13.3	11.1	8.79	15.2	15.5	
Rb	0.00	0.03	1.28	0.03	0.00	0.05	0.81	0.00	0.04	0.01	0.17	0.02	
Sr	54.1	37.9	32.7	23.6	37.7	27.2	41.0	85.4	76.7	52.9	34.6	64.0	
Y	12.1	7.98	23.6	6.74	15.2	7.14	14.5	20.1	17.5	12.4	52.2	26.5	
Zr	22.4	24.0	87.7	21.1	78.9	13.3	41.1	103	51.2	76.6	23.6	87.8	
Nb	0.04	0.02	0.20	0.02	0.06	0.01	0.06	0.07	0.05	0.01	0.03	0.10	
Cs	0.00	0.00	0.29	0.00	0.00	0.03	0.20	0.01	0.00	0.00	0.02	0.00	
Ba	0.05	0.00	1.46	0.00	0.00	0.00	0.63	0.15	0.23	0.22	0.41	0.10	
La	14.0	11.8	33.5	9.9	22.3	10.7	16.5	22.9	17.7	10.5	23.0	24.6	
Ce	44.2	33.6	94.6	26.1	62.7	27.1	50.1	71.7	57.4	33.0	82.8	80.7	
Pr	6.25	4.31	12.7	3.14	8.85	3.39	7.27	10.5	8.39	5.00	13.4	12.3	
Nd	29.8	17.9	53.5	15.6	36.4	14.5	32.8	45.7	37.3	21.0	65.9	55.7	
Sm	5.11	3.58	10.07	3.08	6.32	2.74	6.20	9.16	7.69	4.68	16.42	11.81	
Eu	1.25	0.66	1.94	0.58	1.43	0.54	1.37	2.33	1.77	1.08	2.79	2.49	
Gd	3.64	2.63	7.59	1.72	4.86	2.28	4.62	7.03	6.06	3.83	14.08	9.68	
Tb	0.48	0.31	0.79	0.20	0.56	0.25	0.58	0.89	0.72	0.51	1.99	1.11	
Dy	2.55	1.62	4.57	1.32	2.84	1.41	3.12	4.14	3.41	2.79	10.84	6.02	
Ho	0.37	0.27	0.85	0.20	0.57	0.25	0.50	0.64	0.57	0.40	1.87	0.93	
Er	1.32	0.75	2.39	0.61	1.25	0.82	1.63	1.72	1.64	1.22	4.94	2.69	
Tm	0.18	0.12	0.31	0.09	0.18	0.10	0.16	0.24	0.23	0.20	0.64	0.28	
Yb	1.30	0.99	2.01	0.67	1.20	0.66	1.51	1.39	1.37	1.35	4.18	1.86	
Lu	0.27	0.17	0.38	0.19	0.30	0.17	0.24	0.28	0.25	0.23	0.65	0.30	
Hf	1.51	1.62	5.48	1.27	4.81	0.95	3.00	3.70	2.73	3.21	2.26	5.32	
Ta	0.00	0.00	0.01	0.00	0.01	0.00	0.00	0.08	0.01	0.01	0.00	0.01	
Th	0.04	0.06	0.51	0.12	0.14	0.23	0.27	0.04	0.04	0.04	0.18	0.11	
U	0.01	0.01	0.34	0.03	0.04	0.02	0.07	0.01	0.00	0.01	0.02	0.02	
Data source	Zhou et al. (2020a)							This study					

Notes: b.d.l., below detection limit.

54	55
52.91	52.35
0.22	0.27
0.75	0.75
8.04	8.26
0.33	0.31
13.35	13.38
24.02	24.33
0.63	0.55
0.02	0.01
0.06	0.02
0.03	b.d.l.
b.d.l.	b.d.l.
b.d.l.	b.d.l.
100.34	100.24
0.93	0.72
167	152
0.94	0.79
10.9	10.4
64.4	50.6
77.8	65.8
203	140
338	113
37.4	35.2
96.5	65.8
20.1	12.7
0.00	0.00
69.9	74.6
25.3	23.6
214	108
0.22	0.06
0.00	0.00
0.02	0.00
37.8	23.8
112.2	75.4
14.7	11.0
58.9	47.0
9.39	9.48
2.04	1.87
7.73	7.94
0.89	0.93
4.93	4.79
0.78	0.81
2.28	2.07
0.26	0.23
2.65	1.70
0.43	0.36
6.54	3.68
0.03	0.00
0.13	0.04
0.01	0.01

Table 3. Representative feldspar major and trace element compositions

Pluton	Tonglushan					Tieshan						
	HB008					TS-1	TS-3	HB002	HB004	HB007	HB001	
Sample	24	43	45	46	47	110	206	237	88	163	211	71
Oxide contents (wt %)												
SiO ₂	61.87	53.56	53.56	54.71	55.89	65.44	62.00	63.32	62.67	65.13	62.25	65.11
TiO ₂	b.d.l.	b.d.l.	b.d.l.	b.d.l.	b.d.l.	b.d.l.	0.05	b.d.l.	0.03	b.d.l.	b.d.l.	0.03
Al ₂ O ₃	23.59	28.58	27.47	27.80	27.41	22.56	22.74	23.23	23.03	21.23	23.06	21.42
FeO	0.24	0.17	0.16	0.24	0.26	0.13	0.14	0.10	0.16	0.20	0.14	0.20
MnO	0.01	b.d.l.	b.d.l.	0.03	b.d.l.	b.d.l.	0.03	b.d.l.	0.01	0.04	0.02	b.d.l.
MgO	0.01	0.01	0.03	0.02	b.d.l.	b.d.l.	b.d.l.	b.d.l.	0.01	b.d.l.	b.d.l.	b.d.l.
CaO	5.83	11.93	11.52	11.38	10.51	3.75	4.37	5.06	4.98	3.22	4.74	3.75
Na ₂ O	7.93	4.99	5.04	5.47	5.34	7.42	9.32	8.49	8.47	9.48	8.72	9.55
K ₂ O	0.53	0.15	0.18	0.17	0.19	0.26	0.32	0.30	0.37	0.85	0.34	0.36
P ₂ O ₅	0.01	0.03	0.01	0.01	0.01	0.02	0.02	b.d.l.	0.02	b.d.l.	0.01	b.d.l.
Cr ₂ O ₃	b.d.l.	0.04	0.26	0.35	b.d.l.	b.d.l.	b.d.l.	0.03	0.31	0.00	0.14	b.d.l.
F	b.d.l.	b.d.l.	b.d.l.	b.d.l.	b.d.l.	b.d.l.	b.d.l.	b.d.l.	b.d.l.	b.d.l.	b.d.l.	b.d.l.
Cl	b.d.l.	0.01	b.d.l.	0.00	0.01	0.01	0.00	b.d.l.	0.01	b.d.l.	0.01	b.d.l.
Total	100.01	99.45	98.24	100.17	99.62	99.59	98.98	100.53	100.05	100.15	99.42	100.43
Trace element contents (ppm)												
Cu	0.06	0.29	0.71	0.68	0.40	1.21	0.65	0.76	0.87	0.41	0.38	11.69
Zn	7.47	30.42	6.08	7.21	4.72	3.39	1.27	7.83	6.49	10.1	28.3	2.72
Pb	9.30	4.89	2.90	5.45	5.53	8.78	6.94	7.60	9.44	9.06	12.49	8.34
P	44.2	21.4	19.1	27.9	21.7	3.5	24.8	27.9	12.6	34.1	19.4	14.7
Li	7.26	5.04	0.63	0.91	0.87	2.77	0.00	12.67	7.92	13.06	25.47	2.49
Sc	2.93	2.14	2.13	2.40	1.71	2.61	2.62	3.20	3.39	2.10	3.07	6.12
V	0.20	3.28	0.00	0.04	0.12	0.00	0.00	0.37	0.18	0.02	2.63	0.02
Cr	17.5	31.2	7.4	10.6	12.4	18.0	7.8	10.1	8.6	4.5	6.9	13.1
Co	0.30	1.91	0.22	0.51	0.14	0.13	0.00	0.06	0.07	0.08	0.58	0.10
Ni	3.80	0.00	0.00	0.74	0.00	0.00	0.00	0.00	0.00	0.00	0.00	0.79
Ga	27.6	22.4	20.4	24.3	21.6	29.9	32.6	25.9	26.1	26.5	26.6	29.2
Rb	9.51	1.29	0.71	0.28	0.83	1.47	3.41	0.00	1.05	4.17	11.43	0.78
Sr	1884	2752	2029	2338	1806	1910	1396	4641	3834	3551	3690	1605
Y	0.09	0.29	0.11	0.06	0.03	0.04	0.04	0.18	0.08	0.05	0.06	0.21
Zr	0.00	0.23	0.00	0.00	0.03	0.10	0.00	0.06	0.00	0.00	0.00	0.01
Nb	0.04	0.03	0.01	0.04	0.02	0.13	0.03	0.08	0.00	0.01	0.00	0.23
Cs	0.17	0.18	0.07	0.00	0.07	0.00	0.00	0.00	0.01	0.19	0.63	0.00
Ba	373	187	186	284	554	308	184	363	907	968	518	250
La	9.59	5.73	6.48	6.50	9.67	6.87	4.93	7.51	6.32	4.87	6.78	8.07
Ce	9.46	7.20	7.32	9.50	10.60	4.79	2.22	9.06	5.99	4.20	7.83	4.89
Pr	0.50	0.70	0.48	0.68	0.58	0.18	0.09	0.61	0.29	0.32	0.40	0.20
Nd	0.68	1.83	0.92	1.44	1.71	0.21	0.08	1.82	0.35	0.49	1.49	0.52
Sm	0.15	0.02	0.00	0.11	0.00	0.00	0.00	0.16	0.00	0.04	0.13	0.00
Eu	0.86	0.78	0.57	0.82	0.94	0.64	0.18	0.91	0.90	0.61	0.95	0.42
Gd	0.07	0.08	0.00	0.12	0.06	0.05	0.00	0.07	0.00	0.01	0.03	0.04
Tb	0.00	0.01	0.00	0.00	0.00	0.00	0.00	0.00	0.00	0.01	0.00	0.00
Dy	0.05	0.00	0.00	0.00	0.03	0.00	0.00	0.00	0.02	0.10	0.03	0.00
Ho	0.00	0.01	0.00	0.00	0.00	0.00	0.00	0.01	0.00	0.00	0.01	0.00
Er	0.00	0.00	0.00	0.00	0.00	0.00	0.00	0.00	0.00	0.00	0.00	0.00
Tm	0.00	0.00	0.00	0.00	0.00	0.00	0.00	0.00	0.00	0.00	0.00	0.00
Yb	0.00	0.11	0.02	0.00	0.00	0.04	0.00	0.02	0.00	0.00	0.00	0.00
Lu	0.00	0.00	0.00	0.00	0.00	0.00	0.00	0.01	0.00	0.00	0.01	0.00
Hf	0.02	0.00	0.00	0.03	0.00	0.00	0.00	0.00	0.00	0.00	0.01	0.00
Ta	0.00	0.02	0.02	0.01	0.02	0.19	0.06	0.01	0.00	0.00	0.02	0.34
Th	0.06	0.34	0.00	0.01	0.00	0.00	0.00	0.05	0.00	0.00	0.01	0.00
U	0.04	0.10	0.00	0.00	0.00	0.01	0.00	0.02	0.00	0.01	0.02	0.00
Data source	Zhou et al. (2020a)					Zhou et al. (2020a)						

Notes: b.d.l., below detection limit.

Jinshandian			
JSD-2			
72	82	83	89
64.92	62.20	63.62	63.90
0.01	b.d.l.	b.d.l.	0.02
21.21	23.18	22.49	21.45
0.21	0.16	0.13	0.13
0.01	b.d.l.	b.d.l.	b.d.l.
b.d.l.	b.d.l.	b.d.l.	0.00
3.00	5.17	4.92	4.22
10.07	8.86	9.22	8.18
0.33	0.29	0.22	0.32
0.03	0.00	0.03	b.d.l.
b.d.l.	b.d.l.	b.d.l.	0.20
b.d.l.	b.d.l.	b.d.l.	b.d.l.
b.d.l.	b.d.l.	b.d.l.	b.d.l.
99.78	99.87	100.63	98.41
11.71	11.44	11.69	11.45
3.16	3.57	3.01	3.44
9.40	9.32	8.91	9.78
20.3	19.7	9.9	16.7
4.31	0.00	1.17	0.34
5.24	5.24	5.20	5.01
0.11	0.23	0.00	0.04
9.4	14.7	21.0	18.8
0.06	0.02	0.07	0.01
1.14	0.67	1.21	0.87
27.5	24.8	26.2	25.3
0.71	0.42	1.80	0.70
1622	1866	1839	1865
0.24	0.19	0.07	0.16
0.05	0.00	0.05	0.03
0.18	0.17	0.15	0.15
0.00	0.03	0.04	0.07
440	151	125	267
6.96	7.64	6.02	8.49
4.76	4.78	3.22	5.07
0.19	0.19	0.14	0.20
0.65	0.24	0.25	0.21
0.02	0.00	0.00	0.03
0.72	0.29	0.27	0.46
0.12	0.02	0.00	0.12
0.00	0.00	0.00	0.00
0.00	0.00	0.00	0.00
0.00	0.00	0.00	0.00
0.00	0.00	0.00	0.00
0.00	0.00	0.00	0.00
0.00	0.00	0.00	0.00
0.00	0.00	0.00	0.00
0.00	0.00	0.00	0.00
0.01	0.01	0.00	0.08
0.41	0.23	0.29	0.31
0.00	0.04	0.01	0.02
0.00	0.02	0.01	0.00
This study			

Table 4. Representative amphibole major and trace element compositions

Pluton		Tonglushan					Tieshan						
Sample		HB008					TS-1	TS-3	HB002	HB004	HB007	HB001	
Spot	9	11	21	22	25	132	200	270	79	129	196	1	
Oxide contents (wt %)													
SiO ₂	50.86	51.13	50.97	50.19	50.61	50.03	50.42	47.92	48.91	48.48	48.05	49.39	
TiO ₂	0.77	1.02	0.88	0.94	0.87	0.81	0.70	1.25	1.17	1.20	0.91	0.83	
Al ₂ O ₃	4.73	4.48	4.68	5.02	4.85	5.18	4.29	6.33	5.82	6.06	5.38	4.94	
FeO	11.42	11.45	11.38	11.61	11.34	13.12	13.35	13.44	13.23	13.26	13.13	13.78	
MnO	0.62	0.60	0.54	0.48	0.55	0.38	0.40	0.36	0.47	0.28	0.33	0.18	
MgO	15.56	15.61	15.31	14.93	15.27	13.93	14.22	13.68	13.75	13.79	13.69	14.32	
CaO	11.43	11.70	11.79	12.42	11.67	11.99	11.83	11.56	11.52	11.55	12.06	12.13	
Na ₂ O	1.23	1.25	1.23	1.23	1.16	1.01	1.22	1.51	1.52	1.60	1.48	1.56	
K ₂ O	0.49	0.47	0.49	0.53	0.50	0.58	0.51	0.75	0.68	0.69	0.56	0.70	
P ₂ O ₅	b.d.l.	0.02	b.d.l.	b.d.l.	0.02	b.d.l.	0.01	0.01	0.01	0.02	0.03	0.06	
Cr ₂ O ₃	b.d.l.	0.05	0.02	0.02	0.22	0.03	0.04	0.07	0.06	b.d.l.	0.64	0.03	
F	0.26	0.11	0.15	0.25	0.14	0.21	0.35	0.37	0.26	0.35	0.50	b.d.l.	
Cl	0.10	0.13	0.10	0.11	0.12	0.04	0.08	0.06	0.06	0.11	0.08	0.09	
Total	97.33	97.94	97.45	97.59	97.22	97.21	97.25	97.14	97.32	97.20	96.59	97.98	
Trace element contents (ppm)													
Cu	0.08	0.34	0.18	0.27	0.22	0.53	0.67	0.36	0.32	0.45	1.16	1.85	
Zn	202	175	164	168	170	332	371	308	354	1	324	276	
Pb	0.65	0.38	1.08	1.63	0.25	1.27	0.88	1.16	2.36	4.19	7.50	0.95	
P	4.2	11.6	20.6	13.5	12.5	11.8	14.3	25.1	9.6	0.0	31.3	12.9	
Li	4.08	4.27	2.29	2.94	3.12	13.2	17.3	11.8	28.3	1.4	86.4	15.0	
Sc	67.9	47.3	70.9	75.7	61.7	58.7	49.2	52.9	61.8	2.4	62.0	67.9	
V	150	138	139	167	141	191	180	220	164	0.11	216	199	
Cr	23.1	19.7	17.6	31.3	15.7	32.5	32.6	167	242	1.74	342	170	
Co	52.1	53.8	54.2	52.6	53.4	72.0	74.9	61.9	65.3	0.06	48.5	69.5	
Ni	34.5	38.3	36.5	34.7	34.5	72.0	109	75.1	97.4	2.01	96.2	125	
Ga	18.7	16.9	17.6	21.5	16.7	23.3	23.1	24.7	19.2	21.5	23.4	22.1	
Rb	4.12	3.55	3.43	5.64	3.03	3.69	4.10	1.81	7.35	0.63	21.19	3.87	
Sr	10.2	11.4	12.7	16.0	12.8	73.6	56.3	42.8	44.3	1633.9	93.8	44.2	
Y	41.7	21.9	26.2	39.1	31.8	12.7	8.36	13.0	11.0	0.03	17.0	8.43	
Zr	24.2	20.2	17.6	29.5	18.6	34.6	31.9	45.3	25.6	0.11	42.6	35.6	
Nb	17.6	10.4	10.9	21.2	13.1	18.1	5.99	8.38	5.97	0.00	7.95	7.46	
Cs	0.06	0.00	0.07	0.20	0.03	0.01	0.01	0.00	0.34	0.01	3.40	0.02	
Ba	3.67	2.26	2.88	6.20	5.00	26.4	11.3	31.8	25.8	340	37.0	12.5	
La	35.8	23.5	26.2	46.8	24.8	37.1	20.2	31.0	15.5	5.6	55.9	25.6	
Ce	94.2	55.2	66.1	112.6	67.2	90.3	39.5	63.0	34.0	3.9	62.4	51.7	
Pr	11.9	6.65	8.22	13.49	8.73	12.39	4.05	6.24	4.10	0.16	5.89	5.25	
Nd	53.8	29.5	31.9	52.5	36.9	56.7	16.2	22.4	18.6	0.4	21.9	20.1	
Sm	11.8	6.05	7.243	10.6	8.83	9.23	2.96	4.27	3.51	0.00	5.83	3.08	
Eu	1.73	1.15	1.32	1.60	1.44	1.61	0.77	1.06	0.73	0.20	1.16	1.10	
Gd	9.77	5.19	6.14	8.64	7.23	6.09	2.33	3.77	3.17	0.00	4.85	2.68	
Tb	1.36	0.62	0.75	1.13	0.96	0.68	0.24	0.51	0.36	0.00	0.52	0.35	
Dy	6.51	3.86	4.49	6.54	6.24	2.59	1.33	2.20	2.19	0.03	3.02	1.60	
Ho	1.31	0.68	0.83	1.36	1.05	0.40	0.34	0.36	0.35	0.00	0.56	0.33	
Er	4.21	2.54	2.54	3.41	3.07	1.14	0.82	1.30	1.05	0.05	1.84	0.79	
Tm	0.54	0.25	0.33	0.43	0.41	0.12	0.11	0.11	0.09	0.00	0.32	0.08	
Yb	4.17	2.05	2.32	3.75	2.83	0.66	0.69	0.93	1.09	0.00	1.68	0.59	
Lu	0.55	0.32	0.36	0.63	0.43	0.11	0.13	0.16	0.13	0.00	0.32	0.14	
Hf	2.08	1.36	1.11	2.23	1.41	2.32	1.47	2.65	1.90	0.02	2.27	2.04	
Ta	0.18	0.08	0.10	0.20	0.13	0.34	0.04	0.08	0.05	0.00	0.10	0.06	
Th	0.17	0.08	0.10	0.21	0.10	0.38	0.17	0.09	0.07	0.00	2.32	0.07	
U	0.08	0.06	0.05	0.07	0.05	0.07	0.03	0.01	0.04	0.00	2.82	0.03	
Data source	Zhou et al. (2020a)					Zhou et al. (2020a)							

Notes: b.d.l., below detection limit.

Jinshandian			
JSD-2		JSD-4	
2	3	133	134
49.71	51.78	49.60	50.16
0.88	0.56	1.01	0.85
4.58	3.56	3.71	3.54
13.25	12.05	15.80	15.95
0.19	0.22	0.33	0.34
14.71	15.66	12.88	12.91
12.13	12.38	10.93	11.10
1.49	1.15	2.60	2.50
0.70	0.39	0.71	0.78
b.d.l.	b.d.l.	b.d.l.	b.d.l.
0.06	0.05	0.02	0.01
b.d.l.	b.d.l.	0.80	0.87
0.07	0.05	0.09	0.08
97.76	97.83	98.11	98.70
1.92	1.55	3.32	5.28
279	274	225	208
2.04	0.66	0.52	2.30
12.1	10.1	11.6	13.5
14.9	13.2	12.1	11.6
66.7	57.7	162.9	104.7
189	170	44.0	62.1
141	173	4.88	7.24
70.0	68.4	41.5	37.1
126	133	6.26	8.60
21.3	17.8	32.5	40.2
3.90	3.29	10.72	15.13
44.1	21.8	0.46	7.92
8.38	9.77	360	620
33.8	41.0	235	165
7.25	2.76	104	188
0.03	0.00	0.06	0.01
11.82	4.89	0.22	2.58
24.4	16.9	40.3	48.0
47.6	36.1	165	184
4.85	3.94	26.81	28.97
18.4	15.3	128	127
3.22	3.06	49.5	51.4
1.10	0.68	0.14	0.71
2.96	2.31	59.5	65.7
0.30	0.30	11.2	13.9
1.58	1.40	72.4	96.4
0.26	0.26	12.7	17.7
0.66	0.96	33.4	48.3
0.09	0.13	4.16	6.10
0.81	0.96	26.1	35.7
0.13	0.17	3.61	4.19
1.71	2.51	12.9	15.5
0.04	0.03	2.81	12.05
0.12	0.17	0.26	1.11
0.03	0.03	0.03	0.09
This study			

Table 5. Representative titanite major and trace element compositions

Pluton	Tonglushan								Jinsha			
	HB008 (magmatic)				HB009 (magmatic)				JSD-4 (magmatic)			
Sample	18	s11	s12	s13	s34	s35	s38	s39	138	139	143	145
Oxide contents (wt %)												
SiO ₂	30.21	31.56	31.12	30.17	30.22	30.53	30.75	30.54	30.42	30.41	30.56	30.41
TiO ₂	37.14	37.65	36.76	35.37	34.50	35.84	36.32	36.21	37.09	36.76	36.86	37.14
Al ₂ O ₃	0.91	0.98	1.13	1.08	1.31	1.22	1.98	1.23	0.53	0.42	0.67	0.47
FeO	1.51	1.27	1.49	2.03	2.21	1.95	1.78	1.88	2.43	2.01	1.78	1.82
MnO	0.09	0.17	0.14	0.24	0.18	0.16	0.14	0.16	b.d.l.	b.d.l.	0.02	0.01
MgO	0.01	0.02	0.01	0.03	b.d.l.	0.03	0.02	0.03	0.06	0.03	0.05	0.03
CaO	28.50	27.82	30.25	29.82	30.42	29.19	29.10	29.28	29.15	29.20	29.43	29.66
Na ₂ O	b.d.l.	0.01	b.d.l.	0.02	0.06	0.02	b.d.l.	0.05	0.12	0.10	0.11	0.06
K ₂ O	b.d.l.	b.d.l.	b.d.l.	b.d.l.	b.d.l.	b.d.l.	0.01	0.02	b.d.l.	b.d.l.	0.02	b.d.l.
P ₂ O ₅	0.09	0.07	0.05	0.12	0.09	0.07	0.07	0.08	0.08	0.13	0.08	0.11
Cr ₂ O ₃	b.d.l.	0.04	0.04	b.d.l.	0.06	b.d.l.	0.13	0.01	0.01	b.d.l.	0.01	0.01
F	b.d.l.	0.12	b.d.l.	b.d.l.	b.d.l.	b.d.l.	b.d.l.	b.d.l.	0.19	0.36	0.17	0.07
Cl	0.01	b.d.l.	b.d.l.	b.d.l.	0.01	b.d.l.	b.d.l.	b.d.l.	b.d.l.	b.d.l.	0.01	0.01
Total	98.46	99.66	100.99	98.88	99.05	99.01	100.31	99.48	100.01	99.27	99.69	99.76
Trace element contents (ppm)												
Cu	2.78	3.61	2.83	2.93	2.53	2.39	3.00	2.70	6.18	5.96	6.28	5.93
Zn	7.31	7.86	6.09	13.52	5.70	6.05	6.79	5.09	12.3	12.4	12.3	11.5
Pb	7.48	3.45	3.19	15.57	8.02	5.48	4.82	5.16	4.71	4.97	5.23	4.59
P	243	163	168	517	312	273	342	268	209	248	254	262
Sc	14.8	12.9	13.0	21.8	24.6	19.2	15.9	18.2	17.3	16.6	25.5	25.4
V	660	591	566	597	767	668	614	629	598	598	550	523
Cr	9.77	13.7	12.6	18.4	17.5	14.5	18.1	18.3	11.9	8.92	5.55	5.58
Co	0.20	0.08	0.07	0.73	0.11	0.12	0.12	0.12	0.12	0.08	0.09	0.04
Rb	1.05	0.43	0.08	3.11	0.86	0.31	0.24	0.31	0.87	0.98	0.39	0.37
Sr	10.3	22.4	21.9	17.5	44.0	42.4	42.8	38.9	47.0	49.7	65.4	67.0
Y	2263	778	797	2720	4352	1898	1342	1355	2070	2248	920	902
Zr	693	343	347	2324	1478	1051	643	924	3068	3603	3929	3884
Nb	1857	560	565	3864	2843	1596	1480	1256	2586	2959	1847	1929
Ba	0.38	0.31	0.04	2.23	0.09	0.09	0.08	0.03	0.00	0.03	0.04	0.02
La	5502	1681	1724	7628	4512	3828	3445	3671	1125	1317	1522	1421
Ce	12816	3852	3879	16239	14768	10883	9540	9780	4384	5071	3029	2899
Pr	1372	436	444	1743	2095	1325	1099	1089	605	687	288	282
Nd	5126	1665	1700	6302	8645	4537	3601	3539	2629	2898	1073	1052
Sm	890	269	276	1001	1405	565	433	413	567	618	201	191
Eu	120	67.0	65.7	147	206	141	111	117	29.2	33.8	25.1	25.7
Gd	643	219	218	786	1039	380	287	274	487	519	184	175
Tb	79.9	26.6	27.1	98.7	142	51.6	36.7	36.4	66.5	72.2	25.1	23.9
Dy	445	136	140	514	782	288	203	199	396	426	156	150
Ho	79.2	28.1	28.3	99.4	156	59.7	41.9	41.2	71.6	78.5	30.9	29.7
Er	226	71.4	73.8	261	425	175	122	125	207	225	93.5	89.3
Tm	30.2	10.5	10.9	39.0	63.7	29.0	20.3	21.2	28.0	31.2	13.6	13.2
Yb	219	66.2	66.7	236	367	185	129	140	186	205	94.3	90.7
Lu	29.1	9.95	10.4	34.2	46.7	26.3	19.4	20.6	23.2	24.7	13.9	12.7
Hf	55.5	24.0	25.5	291	99.8	90.5	39.1	77.6	89.0	89.3	164	180
Ta	77.4	14.2	13.7	332	227	106	83.2	69.0	203	211	98.5	107
Th	517	261	265	1040	649	418	343	386	430	468	496	429
U	289	93.7	89.5	382	61.4	44.3	38.5	42.6	26.3	31.7	44.7	42.7
Data source	This study								This s			

Notes: b.d.l., below detection limit.

ndian			
JSD-2 (secondary)			
147	19	20	21
31.02	30.32	30.56	30.43
35.97	37.01	36.88	36.05
0.59	0.78	0.69	1.02
1.76	1.62	1.42	2.29
b.d.l.	0.05	0.03	0.07
0.03	0.03	0.03	0.03
29.72	29.24	28.99	29.51
0.07	0.04	b.d.l.	b.d.l.
b.d.l.	0.02	b.d.l.	b.d.l.
0.07	0.10	0.09	0.04
0.02	0.03	0.01	0.02
0.22	0.22	0.10	0.35
b.d.l.	b.d.l.	b.d.l.	b.d.l.
99.38	99.36	98.74	99.65
6.69	6.12	6.44	6.03
13.3	12.3	12.2	13.4
9.42	6.15	8.74	9.31
382	413	329	291
25.4	12.3	10.9	12.5
698	673	745	670
6.20	139	188	87
0.11	0.16	0.09	0.18
0.51	0.61	0.17	0.18
72.0	76.5	74.9	71.2
1219	259	451	535
2434	962	763	791
2917	797	1018	1540
0.73	0.32	0.06	0.31
2140	2974	3242	4245
4914	4932	6781	9261
475	399	672	961
1663	1141	2475	3441
284	124	337	458
41.3	108	96.2	131
252	88.2	224	295
33.8	8.77	21.3	26.5
213	45.5	98.4	119
40.5	7.7	15.1	19.0
127	23.0	42.6	49.0
17.6	3.21	5.24	5.94
127	25.5	34.9	41.3
18.5	3.74	4.76	5.71
98.0	50.2	51.3	60.3
109	25.9	35.1	44.1
738	438	622	684
97.6	106	148	104
study			

Table 6. Representative apatite major and trace element compositions

Pluton		Tonglushan			
Sample	HB008		HB009		
Spot	s15	s16	s17	s29	s30
Oxide contents (wt %)					
SiO ₂	0.21	0.05	b.d.l.	b.d.l.	0.24
TiO ₂	b.d.l.	b.d.l.	0.07	0.03	b.d.l.
Al ₂ O ₃	b.d.l.	0.00	b.d.l.	0.01	b.d.l.
FeO	0.09	0.08	0.02	0.06	0.06
MnO	0.10	0.10	0.06	0.14	0.11
MgO	0.01	b.d.l.	0.01	b.d.l.	0.00
CaO	54.72	54.93	55.35	54.87	54.65
Na ₂ O	0.00	0.02	0.09	0.07	0.05
K ₂ O	b.d.l.	b.d.l.	b.d.l.	0.01	0.01
P ₂ O ₅	42.80	42.39	42.46	42.36	41.63
Cr ₂ O ₃	0.01	b.d.l.	b.d.l.	b.d.l.	b.d.l.
F	3.20	3.49	3.46	2.85	3.11
Cl	0.37	0.30	0.23	0.50	0.59
Total	100.08	99.82	100.24	99.57	99.01
Trace element contents (ppm)					
Cu	0.70	0.59	0.34	0.36	0.50
Zn	0.51	0.40	0.12	0.54	0.34
Pb	1.54	1.38	1.18	1.03	2.41
V	11.3	10.19	9.48	10.8	17.2
Rb	0.02	0.05	0.02	0.00	0.17
Sr	504	509	511	432	431
Y	199	153	148	156	403
Zr	1.11	0.44	0.45	0.35	2.47
Ba	0.31	0.26	0.10	0.14	0.25
La	2635	2125	2037	1726	3959
Ce	3183	2532	2415	2248	5307
Pr	254	200	190	193	466
Nd	754	580	555	602	1469
Sm	86.9	65.2	62.0	72.2	184
Eu	17.5	13.3	12.8	10.6	26.3
Gd	154	121	114	109	265
Tb	6.63	5.05	4.54	5.34	14.33
Dy	33.8	24.8	23.8	26.9	69.1
Ho	6.51	4.88	4.61	5.01	13.49
Er	18.1	13.4	12.9	14.0	35.3
Tm	2.39	1.81	1.63	1.61	4.36
Yb	14.1	11.5	10.5	10.2	27.0
Lu	2.78	2.00	1.94	1.74	4.72
Th	65.3	65.3	62.2	45.2	177
U	14.0	23.5	24.6	14.4	55.2
Data source	This study				

Notes: b.d.l., below detection limit.

Table 7. Comparison of the Tonglushan, Tieshan, and Jinshandian plutons

	Tonglushan		Tieshan		Jinshandian	
Deposit style	skarn		skarn		skarn	
Metals	Cu-Fe-Au		Fe-Cu		Fe	
Magma properties						
	Rang	Mean	Rang	Mean	Rang	Mean
Whole-rock SiO ₂	62.6–63.7		62.4–64.7		68.2–69.3	
Whole-rock Sr/Y	54–56		88–169		5–18	
Amp(euh) <i>T</i> (°C)	725–809	760±19	728–801	768±16	743–795	763±21
Amp(anh) <i>T</i> (°C)			695–778	747±17	720–783	751±16
Amp(euh) H ₂ O (wt%)	3.4–4.4	3.9±0.2	3.2–4.6	3.9±0.4	1.3–2.0	1.6±0.3
Amp (anh) H ₂ O (wt%)			3.3–4.4	3.8±0.3	2.9–3.9	3.5±0.2
Amp(euh) <i>f</i> O ₂	1.0–2.5	1.7±0.3	1.0–2.1	1.4±0.3	0.9–2.1	1.3±0.4
Amp(anh) <i>f</i> O ₂			1.1–2.2	1.5±0.3	1.1–2.0	1.6±0.2
Mineral Cu contents (ppm)						
	Rang	Mean	Rang	Mean	Rang	Mean
Cpx			0.02–0.94	0.36±0.29	0.65–0.93	0.80±0.08
Ap	0.03–0.70	0.41±0.21				
Pl	0.06–1.31	0.52±0.34	0.03–1.80	0.64±0.42	1.13–12.09	10.6±2.7
Kfs			0.04–1.80	0.69±0.77	1.81–13.0	4.40±3.84
Amp(euh)	0.08–1.15	0.42±0.32	0.10–2.06	0.71±0.52	3.32–5.28	4.19±1.00
Amp(anh)			0.03–1.01	0.28±0.26	1.85–2.23	1.86±0.25
Ttn(mag)	1.83–3.61	2.61±0.50			5.59–6.69	6.03±0.30
Ttn(sec)					5.78–6.66	6.14±0.28

Mineral abbreviations: Amp(euh) = euhedral amphibole, Amp(anh) = anhedral amphibole, Cpx = clinopyroxene, Ap = apatite, Pl = plagioclase, Kfs = K-feldspar, Ttn(mag) = magmatic titanite, Ttn(sec) = secondary titanite.